Geomechanics and Engineering, *Vol. 40, No. 3 (2025) 165-182*
https://doi.org/10.12989/gae.2025.40.3.165

Nonlinear dynamic analysis of concrete gravity dam-water-foundation rock systems utilizing a simplified non-associated elasto-plastic joint model

Vahid Lotfi* and Amin Shiehnezhad[a]

Department of Civil and Environmental Engineering, Amirkabir University of Technology, Tehran, Iran

(*Received January 19, 2023, Revised January 20, 2025, Accepted January 31, 2025*)

Abstract. In the present study, a simplified non-associated joint model is employed to evaluate the influence of apparent friction coefficient and cohesion on earthquake response of concrete gravity dam-water-foundation rock systems. The formulation and its theoretical concepts are discussed initially. Then, a primary verification of the model is considered to control its implementation and to show its characteristics. Thereafter, the sliding behavior of Pine Flat gravity dam-water-foundation rock is studied for different ratios of foundation rock to dam elastic moduli by application of the described nonlinear joint-model. It is shown that joint opening/closing as well as sliding affects the seismic response of gravity dams significantly for rigid foundation assumption case. However, its influence reduces as foundation rock modulus decreases and radiation damping effects increases. This is observed by comparing displacement histories and envelope of principal stresses in dam body. In particular, locations and magnitudes of maximum tensile and compressive stresses occurring in the dam body are also changed when joint modeling is considered in comparison with corresponding linear cases.

Keywords: dam-water-foundation rock interaction; gravity dams; interface elements; non-associated joint model; radiation damping; sliding

1. Introduction

Seismic analysis of dams has attracted many researches in recent years (Lotfi 2004, Karabulut and Genis 2019, Hu and Huang 2019, Nasiri *et al.* 2020, Karalar and Cavusli 2021, Kamalzare *et al.* 2022). Moreover, there have also been many studies to increase the accuracy or efficiency of dynamic analysis of concrete dams. This is mainly related to interaction issues (Basu and Chopra 2003, Samii and Lotfi 2012, Khazaee and Lotfi 2014a, Lokke and Chopra 2018, Lotfi and Zenz 2018, 2019, Lotfi and Lotfi 2021, 2022, Dehghanmarvasty and Lotfi 2023a, b, Lotfi and Abdorazaghi 2024). Another group of studies have concentrated on nonlinear modeling of concrete behavior in dam body (Lee 1996, Lee and Fenves 1998, Lotfi and Omidi 2012, Soysal *et al*. 2016, Omidi and Lotfi 2017, Chen *et al.* 2019, Akbari and Lotfi 2022, Lotfi and Jahanitabar 2024, Soysal and Arici 2024). Joint modeling is also an essential part of seismic analysis of concrete dams. For concrete arch dams, this is utilized for modeling of contraction joints (Fenves *et al.* 1989, Fenves *et al.* 1992, Ahmadi and Razavi 1992, Ahmadi *et al*. 2001), and less often for modeling of both contraction joints and peripheral joint (Lotfi and Espandar 2002, Lotfi and Espandar 2004, Omidi and Lotfi 2017). In these studies, researchers have utilized relatively simple joint models in three-dimensional context which mainly consider joint opening and closure while assuming linear behavior for shear stresses. It should be noted that this assumption is acceptable for contraction joints if shear keys exist and there is no damage induced during their seismic experience. Moreover, slightly different joint model was employed for peripheral joint. The main difference was that shear stresses are released during joint opening process. Of course, it regains its stiffness in all three directions if the normal stress at the Gauss point tries to move into the compression range at a later stage. There are also plasticity based joint models which have been employed for nonlinear seismic analysis of concrete arch dams (Ghabousi *et al.* 1973, Hohberg 1991, Hohberg 1992, Lau *et al*. 1998, Azmi and Paultre 2002, Arabshahi and Lotfi 2009). However, there are usually more possibilities for divergence problems in more complicated models. Similar simple or complicated models in two-dimensional context were also employed for seismic analysis of concrete gravity dams (Leger and Katsouli 1989, Hall *et al*. 1991, Arabshahi and Lotfi 2008).

There is also a famous program (i.e., EAGD-SLIDE) developed especially for sliding analysis of concrete gravity dams (Chaves and Fenves 1993) which its sliding model is based upon limit equilibrium approaches relying on Mohr-Coulomb relation. Although, this is considered an advanced software due to its capabilities in including dam-water interaction and dam-foundation rock interaction based on enhanced approaches, there are two main limitations in its joint model. These are related to the fact that joint opening/closing is neglected and the assumption that cohesion is disregarded.

In the present study, a plasticity based non-associated joint model is employed for seismic analysis of concrete gravity dam-water-foundation rock systems. It should be

*Corresponding author, Professor
E-mail: vahlotfi@aut.ac.ir
[a]M.Sc. Student

http://www.techno-press.org/?journal=gae&subpage=7
ISSN: 2005-307X (Print), 2092-6219 (Online)

emphasized that this was initially proposed and investigated in the context of rigid foundation assumption in a preceding study (Lotfi and Shiehnezhad 2023). In this model, certain assumptions are imposed to make the implementation of the model relatively simple and straight forward. Moreover, the present experience reveals again that possibility of divergence is nil. It is also worthwhile to mention that it is based on a perfect plastic type model with hyperbolic yield function. This model is relying on two coefficients which can be referred to as apparent friction coefficient and cohesion. Therefore, it can be utilized to study the influence of both apparent friction coefficient as well as apparent cohesion on earthquake response of gravity dams. Additionally, it should be emphasized that joint opening/closing possibility is also included in this model.

The formulation and its theoretical concepts are discussed initially. Then, a primary verification of the model is considered to control its implementation and to show its characteristics. Thereafter, the sliding behavior of Pine Flat gravity dam-water-foundation rock is studied for different ratios of foundation rock to dam elastic moduli by application of this simplified nonlinear joint-model. It is shown that joint opening/closing as well as sliding affects the seismic response of gravity dams significantly for rigid foundation assumption case. However, its influence reduces as foundation rock modulus decreases and radiation damping effects increases.

This is observed by comparing displacement histories and envelope of principal stresses in dam body. In particular, locations and magnitudes of maximum tensile and compressive stresses occurring in the dam body are also changed when joint modeling is considered in comparison with corresponding linear cases.

2. Simplified non-associated elasto-plastic joint model

2.1 Elasto-plastic rigidity matrix

In this section, the elasto-plastic rigidity matrix is derived for interface elements.

For the elastic region, the elastic rigidity matrix defines the relation between the differential strain and stress vectors as below:

$$\mathrm{d}\boldsymbol{\sigma}^{\mathrm{e}} = \mathbf{D}^{\mathrm{e}}\mathrm{d}\boldsymbol{\epsilon} \tag{1}$$

The differential stress vector consists of shear and normal stress components

$$\mathrm{d}\boldsymbol{\sigma}^{\mathrm{e}} = (\mathrm{d}\tau_{\mathrm{r}}^{\mathrm{e}} \quad \mathrm{d}\sigma_{\mathrm{n}}^{\mathrm{e}})^{\mathrm{T}} \tag{2}$$

Similarly for the differential strain components

$$\mathrm{d}\boldsymbol{\epsilon} = (\mathrm{d}\gamma_{nr} \quad \mathrm{d}\epsilon_{\mathrm{n}})^{\mathrm{T}} \tag{3a}$$

Of course, it needs to be emphasized that these strain components are essentially the relative tangential and normal displacements between the two surfaces of interface element at that point. This is due to the fact that a zero thickness element is utilized herein. Therefore, it can also be written as

$$\mathrm{d}\boldsymbol{\epsilon} = (\mathrm{du}_{\mathrm{r}} \quad \mathrm{du}_{\mathrm{n}})^{\mathrm{T}} \tag{3b}$$

The elastic rigidity is in general a full 2×2 matrix. However, it is usually simplified as a diagonal matrix as follows (Lotfi and Espandar 2002)

$$\mathbf{D}^{\mathrm{e}} = \begin{bmatrix} \mathrm{k}_{\mathrm{r}} & 0 \\ 0 & \mathrm{k}_{\mathrm{n}} \end{bmatrix} \tag{4}$$

Where k_{r} , k_{n} denote the distributed tangential and normal stiffness connecting two surfaces of interface element. Of course, the relation (1) is not valid anymore when the behavior shifts into the elasto-plastic region. However, a similar relation may be written by employing the extracted differential elastic strain which is the difference of total and plastic differential strain:

$$\mathrm{d}\boldsymbol{\sigma} = \mathbf{D}^{\mathrm{e}}\mathrm{d}\boldsymbol{\epsilon}^{\mathrm{e}} \tag{5a}$$

$$\mathrm{d}\boldsymbol{\sigma} = \mathbf{D}^{\mathrm{e}}(\mathrm{d}\boldsymbol{\epsilon} - \mathrm{d}\boldsymbol{\epsilon}^{\mathrm{p}}) \tag{5b}$$

Moreover, the differential plastic strain is defined by the help of plastic potential function G in the more general non-associated flow rule assumption adopted herein

$$\mathrm{d}\boldsymbol{\epsilon}^{\mathrm{p}} = \mathbf{b}\,\mathrm{d}\lambda \tag{6a}$$

$$\mathbf{b} = \frac{\partial \mathrm{G}}{\partial \boldsymbol{\sigma}} \tag{6b}$$

Substituting Eq. (6(a)) into (5(b)) yields

$$\mathrm{d}\boldsymbol{\sigma} = \mathbf{D}^{\mathrm{e}}\mathrm{d}\boldsymbol{\epsilon} - \mathbf{D}^{\mathrm{e}}\mathbf{b}\,\mathrm{d}\lambda \tag{7}$$

In the present study, the yield surface is defined by a hyperbolic function as below

$$\mathrm{F} = \sqrt{\tau_{\mathrm{r}}^2 + \mathrm{c}^2} + \mu\,\sigma_{\mathrm{n}} - \mathrm{c} = 0 \tag{8}$$

Where c, μ can be interpreted as the apparent cohesion and friction coefficient (i.e., tangent of friction angle). It is also worthwhile to mention that Mohr-Coulomb type function with similar c, μ parameters, which are actual cohesion and friction coefficient in that case, acts as the asymptote of the present hyperbolic type function.

Thereafter, the consistency condition is written based on the perfect plastic assumption adopted herein.

$$\left(\frac{\partial \mathrm{F}}{\partial \boldsymbol{\sigma}}\right)^{\mathrm{T}} \mathrm{d}\boldsymbol{\sigma} = 0 \tag{9}$$

This may also be written as follows by employing a vector which is related to yield function

$$\mathbf{a}^{\mathrm{T}}\mathrm{d}\boldsymbol{\sigma} = 0 \tag{10a}$$

$$\mathbf{a} = \left[\frac{\partial \mathrm{F}}{\partial \tau_{\mathrm{r}}} \quad \frac{\partial \mathrm{F}}{\partial \sigma_{\mathrm{n}}}\right]^{\mathrm{T}} \tag{10b}$$

$$\mathbf{a} = [\beta \quad \mu]^{\mathrm{T}} \qquad ; \qquad \beta = \frac{\tau_{\mathrm{r}}}{\sqrt{\tau_{\mathrm{r}}^2 + \mathrm{c}^2}} \tag{10c}$$

It should be noted that parameter β utilized above is variable. However, μ is a constant coefficient.

Substituting $\mathrm{d}\boldsymbol{\sigma}$ from Eq. (7) into Eq. (10(a)) results in

$$\mathbf{a}^{\mathrm{T}}(\mathbf{D}^{\mathrm{e}}\mathrm{d}\boldsymbol{\epsilon} - \mathbf{D}^{\mathrm{e}}\mathbf{b}\,\mathrm{d}\lambda) = 0 \tag{11}$$

Which can now be solved for the differential of consistency parameter dλ

$$\mathrm{d}\lambda = \frac{\mathbf{a}^{\mathrm{T}}\mathbf{D}^{\mathrm{e}}\mathrm{d}\boldsymbol{\epsilon}}{\mathbf{a}^{\mathrm{T}}\mathbf{D}^{\mathrm{e}}\mathbf{b}} \tag{12}$$

This is now replaced in Eq. (7) to define elasto-plastic rigidity matrix as follows:

$$\mathrm{d}\boldsymbol{\sigma} = \mathbf{D}^{\mathrm{ep}}\mathrm{d}\boldsymbol{\epsilon} \tag{13a}$$

$$\mathbf{D}^{\mathrm{ep}} = \mathbf{D}^{\mathrm{e}} - \frac{\mathbf{D}^{\mathrm{e}}\mathbf{b}\,\mathbf{a}^{\mathrm{T}}\mathbf{D}^{\mathrm{e}}}{\mathbf{a}^{\mathrm{T}}\mathbf{D}^{\mathrm{e}}\mathbf{b}} \tag{13b}$$

This matrix may also be simplified as follows

$$\mathbf{D}^{\mathrm{ep}} = \mathbf{D}^{\mathrm{e}} - \frac{\mathbf{d}_{\mathrm{b}}\,\mathbf{d}_{\mathrm{a}}^{\mathrm{T}}}{\mathbf{a}^{\mathrm{T}}\mathbf{d}_{\mathrm{b}}} \tag{14}$$

With the following definitions for employed vectors:

$$\mathbf{d}_{\mathrm{a}} = \mathbf{D}^{\mathrm{e}}\mathbf{a} \tag{15a}$$

$$\mathbf{d}_{\mathrm{b}} = \mathbf{D}^{\mathrm{e}}\mathbf{b} \tag{15b}$$

Moreover, it should be mentioned that a Mohr-Coulomb type plastic potential function is adopted in the present model which may be written as

$$\mathrm{G} = |\tau_{\mathrm{r}}| + \mu_{\mathrm{g}}\,\sigma_{\mathrm{n}} - \mathrm{c} = 0 \tag{16}$$

Subsequently, the **b** vector can be defined through Eqs. (6(b)) and (16) as follows

$$\mathbf{b} = \left[\frac{\partial \mathrm{G}}{\partial \tau_{\mathrm{r}}} \quad \frac{\partial \mathrm{G}}{\partial \sigma_{\mathrm{n}}}\right]^{\mathrm{T}} \tag{17a}$$

$$\mathbf{b} = [\mathrm{I_s} \quad \mu_{\mathrm{g}}]^{\mathrm{T}} \qquad ;\ \mathrm{I_s} = \mathrm{Isign}(\tau_{\mathrm{r}}) \tag{17b}$$

Thereafter, $\mathbf{d}_{\mathrm{a}}$, $\mathbf{d}_{\mathrm{b}}$ vectors are obtained by utilizing Eqs. (10(c)), (15) and (17(b))

$$\mathbf{d}_{\mathrm{a}} = [\mathrm{k_r}\beta \quad \mathrm{k_n}\mu]^{\mathrm{T}} \tag{18a}$$

$$\mathbf{d}_{\mathrm{b}} = [\mathrm{k_r}\mathrm{I_s} \quad \mathrm{k_n}\mu_{\mathrm{g}}]^{\mathrm{T}} \tag{18b}$$

These vectors are now replaced in Eq. (14) to define the elasto-plastic rigidity matrix.

$$\mathbf{D}^{\mathrm{ep}} = \begin{bmatrix}\mathrm{k_r} & 0\\ 0 & \mathrm{k_n}\end{bmatrix} - \frac{1}{(\mathrm{k_r}\beta\mathrm{I_s} + \mathrm{k_n}\mu\mu_{\mathrm{g}})}\begin{bmatrix}\mathrm{k_r^2}\beta\mathrm{I_s} & \mathrm{k_r}\mathrm{k_n}\mu\mathrm{I_s}\\ \mathrm{k_r}\mathrm{k_n}\beta\mu_{\mathrm{g}} & \mathrm{k_n^2}\mu\mu_{\mathrm{g}}\end{bmatrix} \tag{19}$$

This is the elasto-plastic rigidity matrix in its general form for the interface element. However, it may be simplified by setting $\mu_{\mathrm{g}} = 0$ as in the present study

$$\mathbf{D}^{\mathrm{ep}} = \begin{bmatrix}\mathrm{k_r} & 0\\ 0 & \mathrm{k_n}\end{bmatrix} - \frac{1}{(\mathrm{k_r}\beta\mathrm{I_s})}\begin{bmatrix}\mathrm{k_r^2}\beta\mathrm{I_s} & \mathrm{k_r}\mathrm{k_n}\mu\mathrm{I_s}\\ 0 & 0\end{bmatrix} \tag{20}$$

Alternatively, it may be written as below

$$\mathbf{D}^{\mathrm{ep}} = \begin{bmatrix}0 & -\frac{\mu}{\beta}\\ 0 & 1\end{bmatrix}\mathrm{k_n} \tag{21}$$

This simplified rigidity matrix is valid at Gauss points with yielding behavior and it can be utilized for defining the tangent stiffness matrix.

2.2 Stress calculation procedure

The elasto-plastic rigidity matrix was defined in the previous section (i.e., Eq. (21)) which relates the differential stress and strain vector through Eq. (13(a)) at each Gauss point with nonlinear behavior. This leads to the following relation for differential stress vector:

$$\mathrm{d}\boldsymbol{\sigma} = \begin{bmatrix}-\frac{\mu}{\beta}\\ 1\end{bmatrix}\mathrm{d}\sigma_{\mathrm{n}}^{\mathrm{e}} \tag{22a}$$

$$\mathrm{d}\sigma_{\mathrm{n}}^{\mathrm{e}} = \mathrm{k_n}\mathrm{d}\epsilon_{\mathrm{n}} \tag{22b}$$

Of course, in practical applications, one requires to integrate this relation for a finite strain increment. This can be achieved by dividing each finite strain vector or alternatively elastic stress vector by several steps (i.e., MSTEP) and carry out the integration process as usual in the elasto-plastic models. However, this lengthy process can be avoided as it is described below.

2.2.1 The second alternative for stress calculation

As mentioned, the first alternative in stress calculation was to integrate Eq. (22(a)) by usual approach in elasto-plastic models. However, it is noticed through Eq. (22) that the second component of differential stress vector can be easily integrated and results in

$$\Delta\sigma_{\mathrm{n}} = \Delta\sigma_{\mathrm{n}}^{\mathrm{e}} \tag{23a}$$

$$\Delta\sigma_{\mathrm{n}}^{\mathrm{e}} = \mathrm{k_n}\Delta\epsilon_{\mathrm{n}} \tag{23b}$$

Therefore, the normal stress component at iterations i and i+1 are simply written as

$$\sigma_{\mathrm{n}}^{\mathrm{i+1}} = \sigma_{\mathrm{n}}^{\mathrm{i}} + \Delta\sigma_{\mathrm{n}} \tag{24}$$

Subsequently, one can obtain the shear stress component in such a manner that stress point satisfies the hyperbolic yield function (i.e., Eq. (8)). It leads to the following relation

$$\tau_{\mathrm{r}}^{\mathrm{i+1}} = \pm\sqrt{(\mathrm{c} - \mu\sigma_{\mathrm{n}}^{\mathrm{i+1}})^2 - \mathrm{c}^2} \tag{25}$$

Of course, there is an ambiguity in regard to the sign of the shear stress component. This can be resolved by defining the trial shear stress assuming linear behavior as follows

$$\tau_{\mathrm{r}}^{\mathrm{trial}} = \tau_{\mathrm{r}}^{\mathrm{i}} + \Delta\tau_{\mathrm{r}}^{\mathrm{e}} \tag{26a}$$

$$\Delta\tau_{\mathrm{r}}^{\mathrm{e}} = \mathrm{k_r}\Delta\epsilon_{\mathrm{r}} \tag{26b}$$

The actual shear stress has similar sign as the trial shear stress. Therefore, the final clear form of shear stress may be calculated as below

$$\tau_{\mathrm{r}}^{\mathrm{i+1}} = \left(\sqrt{(\mathrm{c} - \mu\sigma_{\mathrm{n}}^{\mathrm{i+1}})^2 - \mathrm{c}^2}\right)\ \mathrm{Isign}(\tau_{\mathrm{r}}^{\mathrm{trial}}) \tag{27}$$

Therefore, one can define the stress vector at iteration i+1 as

$$\boldsymbol{\sigma}^{i+1} = \begin{bmatrix} \tau_r^{i+1} \\ \sigma_n^{i+1} \end{bmatrix} \tag{28}$$

2.2.2 Joint opening and closure treatment

There is also possibility of joint opening and subsequent closure which needs to be taken into account. The positive value of normal strain (i.e., $\epsilon_n > 0$) corresponds to joint opening. Therefore, the stress vector can be set equal to zero under that condition. Moreover, if the joint is open and it is closing at certain step, the portion of strain which induces stress must be calculated (i.e., RFACT $= \epsilon_n/\Delta\epsilon_n$). This factor can be applied directly on the initial elastic stress vector to obtain the true elastic stress vector.

Based on the above explanations, the simplified stress calculation algorithm can be summarized. This is carried out and presented in a pertinent previous study (Lotfi and Shiehnezhad 2023).

3. Formulation of concrete gravity dam-water-foundation rock system

The dynamic equilibrium equation of dam-water system can be written as follows

$$\begin{bmatrix} \mathbf{M}_{dd} & \mathbf{M}_{db} \\ \mathbf{M}_{db}^T & \mathbf{M}_{bb} \end{bmatrix} \begin{bmatrix} \ddot{\mathbf{U}}_d^t \\ \ddot{\mathbf{U}}_b^t \end{bmatrix} + \begin{bmatrix} \mathbf{C}_{dd} & \mathbf{C}_{db} \\ \mathbf{C}_{db}^T & \mathbf{C}_{bb} \end{bmatrix} \begin{bmatrix} \dot{\mathbf{U}}_d^t \\ \dot{\mathbf{U}}_b^t \end{bmatrix} + \begin{bmatrix} \mathbf{K}_{dd} & \mathbf{K}_{db} \\ \mathbf{K}_{db}^T & \mathbf{K}_{bb} \end{bmatrix} \begin{bmatrix} \mathbf{U}_d^t \\ \mathbf{U}_b^t \end{bmatrix} = \begin{bmatrix} \mathbf{0} \\ \mathbf{R}_b \end{bmatrix} \tag{29}$$

Where $\mathbf{M}$, $\mathbf{C}$, $\mathbf{K}$ represent mass, damping and stiffness matrices of the system, respectively. It should be emphasized that mass matrix $\mathbf{M}$ includes the added mass resulting from hydrodynamic pressures (Kuo 1982). This is often utilized to simplify the dam-water interaction. Furthermore, $\mathbf{U}^t$ denotes total displacement vector which is partitioned into degrees of freedom corresponding to nodes above and on the base (d and b) of the dam. In this manner, $\mathbf{R}_b$ represent the reacting force vector at the base of the dam.

Based on the added motion formulation (also referred to as SSI approach (Wilson 2002)), total displacement vector $\mathbf{U}^t$ may be written as the sum of free field and scattered displacement vectors ($\mathbf{U}^f$ and $\mathbf{U}$).

$$\begin{bmatrix} \mathbf{U}_d^t \\ \mathbf{U}_b^t \end{bmatrix} = \begin{bmatrix} \mathbf{U}_d^f \\ \mathbf{U}_b^f \end{bmatrix} + \begin{bmatrix} \mathbf{U}_d \\ \mathbf{U}_b \end{bmatrix} \; ; \qquad \begin{bmatrix} \mathbf{U}_d^f \\ \mathbf{U}_b^f \end{bmatrix} = \begin{bmatrix} \mathbf{J}_d \\ \mathbf{J}_b \end{bmatrix} \mathbf{u}_g \tag{30}$$

It should be mentioned that $\mathbf{U}^f$ vector in the dam region may be written in terms of ground surface free field displacement vector $\mathbf{u}_g$ and the influence matrix $\mathbf{J}$. This is due to uniform ground motion assumption at the base of the dam. Moreover, $\mathbf{J}$ is a matrix with two columns and every two rows is a 2×2 identity matrix. Therefore, its columns represent unit rigid body motion in horizontal and vertical directions. By utilizing Eq. (30), its time derivatives and replacing them in Eq. (29), one obtains

$$\begin{bmatrix} \mathbf{M}_{dd} & \mathbf{M}_{db} \\ \mathbf{M}_{db}^T & \mathbf{M}_{bb} \end{bmatrix} \begin{bmatrix} \ddot{\mathbf{U}}_d \\ \ddot{\mathbf{U}}_b \end{bmatrix} + \begin{bmatrix} \mathbf{C}_{dd} & \mathbf{C}_{db} \\ \mathbf{C}_{db}^T & \mathbf{C}_{bb} \end{bmatrix} \begin{bmatrix} \dot{\mathbf{U}}_d \\ \dot{\mathbf{U}}_b \end{bmatrix} + \begin{bmatrix} \mathbf{K}_{dd} & \mathbf{K}_{db} \\ \mathbf{K}_{db}^T & \mathbf{K}_{bb} \end{bmatrix} \begin{bmatrix} \mathbf{U}_d \\ \mathbf{U}_b \end{bmatrix} = \begin{bmatrix} \mathbf{0} \\ \mathbf{R}_b \end{bmatrix} - \begin{bmatrix} \mathbf{M}_{dd} & \mathbf{M}_{db} \\ \mathbf{M}_{db}^T & \mathbf{M}_{bb} \end{bmatrix} \begin{bmatrix} \mathbf{J}_d \\ \mathbf{J}_b \end{bmatrix} \mathbf{a}_g(t) \tag{31}$$

It is worthwhile to mention that stiffness and damping matrices multiplied by columns of influence matrix $\mathbf{J}$ (representing rigid body motions) result in null vectors and this fact is also employed in derivation of Eq. (31).

In a similar manner, the dynamic equilibrium equation of foundation rock region can be written as follows

$$\begin{bmatrix} \mathbf{M}_{cc} & \mathbf{M}_{cf} \\ \mathbf{M}_{cf}^T & \mathbf{M}_{ff} \end{bmatrix} \begin{bmatrix} \ddot{\mathbf{U}}_c^t \\ \ddot{\mathbf{U}}_f^t \end{bmatrix} + \begin{bmatrix} \mathbf{C}_{cc} & \mathbf{C}_{cf} \\ \mathbf{C}_{cf}^T & \mathbf{C}_{ff} \end{bmatrix} \begin{bmatrix} \dot{\mathbf{U}}_c^t \\ \dot{\mathbf{U}}_f^t \end{bmatrix} + \begin{bmatrix} \mathbf{K}_{cc} & \mathbf{K}_{cf} \\ \mathbf{K}_{cf}^T & \mathbf{K}_{ff} \end{bmatrix} \begin{bmatrix} \mathbf{U}_c^t \\ \mathbf{U}_f^t \end{bmatrix} = \begin{bmatrix} \mathbf{R}_c \\ \mathbf{0} \end{bmatrix} \tag{32}$$

It is noted that total displacement vector is utilized again which is partitioned into degrees of freedom corresponding to nodes located adjacent to the base of the dam and the remaining nodes of foundation rock region (c and f). In this manner, $\mathbf{R}_c$ represents the reacting force vector at the top of the foundation rock corresponding to c nodes.

The total displacement vector in the foundation rock region can also be divided into two parts as below

$$\begin{bmatrix} \mathbf{U}_c^t \\ \mathbf{U}_f^t \end{bmatrix} = \begin{bmatrix} \mathbf{U}_c^f \\ \mathbf{U}_f^f \end{bmatrix} + \begin{bmatrix} \mathbf{U}_c \\ \mathbf{U}_f \end{bmatrix} \tag{33}$$

It is also known that the following relation holds for the free field motion in that region

$$\begin{bmatrix} \mathbf{M}_{cc} & \mathbf{M}_{cf} \\ \mathbf{M}_{cf}^T & \mathbf{M}_{ff} \end{bmatrix} \begin{bmatrix} \ddot{\mathbf{U}}_c^f \\ \ddot{\mathbf{U}}_f^f \end{bmatrix} + \begin{bmatrix} \mathbf{C}_{cc} & \mathbf{C}_{cf} \\ \mathbf{C}_{cf}^T & \mathbf{C}_{ff} \end{bmatrix} \begin{bmatrix} \dot{\mathbf{U}}_c^f \\ \dot{\mathbf{U}}_f^f \end{bmatrix} + \begin{bmatrix} \mathbf{K}_{cc} & \mathbf{K}_{cf} \\ \mathbf{K}_{cf}^T & \mathbf{K}_{ff} \end{bmatrix} \begin{bmatrix} \mathbf{U}_c^f \\ \mathbf{U}_f^f \end{bmatrix} = \begin{bmatrix} \mathbf{0} \\ \mathbf{0} \end{bmatrix} \tag{34}$$

By utilizing Eqs. (33) and (34), one can transform Eq. (32) to the following relation

$$\begin{bmatrix} \mathbf{M}_{cc} & \mathbf{M}_{cf} \\ \mathbf{M}_{cf}^T & \mathbf{M}_{ff} \end{bmatrix} \begin{bmatrix} \ddot{\mathbf{U}}_c \\ \ddot{\mathbf{U}}_f \end{bmatrix} + \begin{bmatrix} \mathbf{C}_{cc} & \mathbf{C}_{cf} \\ \mathbf{C}_{cf}^T & \mathbf{C}_{ff} \end{bmatrix} \begin{bmatrix} \dot{\mathbf{U}}_c \\ \dot{\mathbf{U}}_f \end{bmatrix} + \begin{bmatrix} \mathbf{K}_{cc} & \mathbf{K}_{cf} \\ \mathbf{K}_{cf}^T & \mathbf{K}_{ff} \end{bmatrix} \begin{bmatrix} \mathbf{U}_c \\ \mathbf{U}_f \end{bmatrix} = \begin{bmatrix} \mathbf{R}_c \\ \mathbf{0} \end{bmatrix} \tag{35}$$

The nonlinearity of the problem corresponds to interface elements located at dam-foundation rock interface. As discussed above, this may arise due to sliding or joint opening. The equilibrium equation for this part may be written as follows

$$\begin{bmatrix} \mathbf{F}_b^{int} \\ \mathbf{F}_c^{int} \end{bmatrix} = \begin{bmatrix} -\mathbf{R}_b \\ -\mathbf{R}_c \end{bmatrix} \tag{36}$$

It is noted that pertinent vectors in this part are partitioned as b and c. This is due to the fact that interface nodes at the top and bottom layers are connected to b nodes of the dam and c nodes of the foundation rock region, respectively. Therefore, reacting forces of interface elements part are opposite to the connecting portions (dam-water and foundation rock region). It is also emphasized that internal force vector is denoted by $\mathbf{F}^{int}$ and there are no mass and damping matrices considered for interface elements.

By combining Eqs. (31), (35) and (36), it leads to the dynamic equilibrium of dam-water-foundation rock system including nonlinear interface elements

$$\mathbf{M}\,\ddot{\mathbf{U}} + \mathbf{C}\,\dot{\mathbf{U}} + \mathbf{K}\,\mathbf{U} + \mathbf{F}^{int} = \mathbf{R}^{st} - \bar{\mathbf{M}}\,\bar{\mathbf{J}}\,\mathbf{a}_g(t) \tag{37}$$

With the following matrix definitions for the complete system

$$= \begin{bmatrix} \mathbf{M}_{dd} & \mathbf{M}_{db} & \mathbf{0} \\ \mathbf{M}_{db}^{T} & \mathbf{M}_{bb} & \\ \mathbf{0} & & \begin{matrix} \mathbf{M}_{cc} & \mathbf{M}_{cf} \\ \mathbf{M}_{cf}^{T} & \mathbf{M}_{ff} \end{matrix} \end{bmatrix}; \mathbf{C} = \begin{bmatrix} \mathbf{C}_{dd} & \mathbf{C}_{db} & \mathbf{0} \\ \mathbf{C}_{db}^{T} & \mathbf{C}_{bb} & \\ \mathbf{0} & & \begin{matrix} \mathbf{C}_{cc} & \mathbf{C}_{cf} \\ \mathbf{C}_{cf}^{T} & \mathbf{C}_{ff} \end{matrix} \end{bmatrix};$$

$$\mathbf{K} = \begin{bmatrix} \mathbf{K}_{dd} & \mathbf{K}_{db} & \mathbf{0} \\ \mathbf{K}_{db}^{T} & \mathbf{K}_{bb} & \\ \mathbf{0} & & \begin{matrix} \mathbf{K}_{cc} & \mathbf{K}_{cf} \\ \mathbf{K}_{cf}^{T} & \mathbf{K}_{ff} \end{matrix} \end{bmatrix} \tag{38}$$

$$\mathbf{U} = \begin{bmatrix} \mathbf{U}_d \\ \mathbf{U}_b \\ \mathbf{U}_c \\ \mathbf{U}_f \end{bmatrix}; \mathbf{F}^{int} = \begin{bmatrix} \mathbf{0} \\ \mathbf{F}_b^{int} \\ \mathbf{F}_c^{int} \\ \mathbf{0} \end{bmatrix}; \overline{\mathbf{M}} = \begin{bmatrix} \mathbf{M}_{dd} & \mathbf{M}_{db} & \mathbf{0} \\ \mathbf{M}_{db}^{T} & \mathbf{M}_{bb} & \\ \mathbf{0} & & \begin{matrix} \mathbf{0} & \mathbf{0} \\ \mathbf{0} & \mathbf{0} \end{matrix} \end{bmatrix};$$

$$\bar{\mathbf{J}} = \begin{bmatrix} \mathbf{J}_d \\ \mathbf{J}_b \\ \mathbf{J}_c \\ \mathbf{J}_f \end{bmatrix}; \ \mathbf{R}^{st} = \begin{bmatrix} \mathbf{R}_d^{st} \\ \mathbf{R}_b^{st} \\ \mathbf{0} \\ \mathbf{0} \end{bmatrix} \tag{39}$$

It should be mentioned that $\mathbf{R}^{st}$ is also included as a load vector on the right hand side of Eq. (37) to generalize it. This vector represents static forces due to dam body weight, hydrostatic pressures acting on the upstream face of the dam and uplift pressures at the base of the dam.

The relation (37) may also be rewritten as below

$$\mathbf{M}\,\ddot{\mathbf{U}} + \mathbf{P}\left(\mathbf{U}, \dot{\mathbf{U}}\right) = \mathbf{R} \tag{40}$$

With the following vector definitions

$$\mathbf{P}\left(\mathbf{U}, \dot{\mathbf{U}}\right) = \mathbf{C}\,\dot{\mathbf{U}} + \mathbf{K}\,\mathbf{U} + \mathbf{F}^{int} \tag{41}$$

$$\mathbf{R} = \mathbf{R}^{st} - \overline{\mathbf{M}}\,\bar{\mathbf{J}}\,\mathbf{a}_g(t) \tag{42}$$

It is worthwhile to emphasize that resulting Eq. (40) is solved incrementally. The static forces are applied in the negative range of time. Dam body weight is applied initially, followed by hydrostatic and uplift pressures. Subsequently, the earthquake excitation is imposed in the positive range of time.

It is apparent that there are no inertia and damping forces during static analysis. Moreover, stiffness matrix $\mathbf{K}$ include spring stiffness's placed at the bottom, left and right side of foundation rock region during static analysis. At time zero, end of static analysis, these springs are removed while a constant internal force vector remains afterwards due to the effect of these springs at time zero. It is also noted that damping matrix $\mathbf{C}$ includes the distributed damping effects related to Lysmer boundary condition at the bottom, left and right side of foundation rock region imposed in the problem for the positive range of time (i.e., dynamic analysis). The solution to Eq. (40) is carried out through HHT-α procedure explained elsewhere in details (Lotfi and Shiehnezhad 2023).

4. Verification example

For an initial verification of the model, the following example has been defined:

Let us consider a single 6-node isoparametric interface element (Fig. 1(a)). The basic material data for this element include the normal stiffness coefficient $k_n = 136.5$ GPa/m, and tangential stiffness coefficient is taken about one half of normal component. Moreover, apparent cohesion and friction coefficient are taken as $c = 1.0$ MPa and $\mu = 1.0$, respectively.

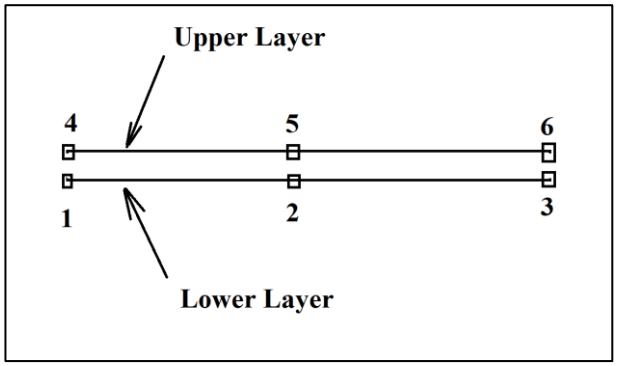

(a)

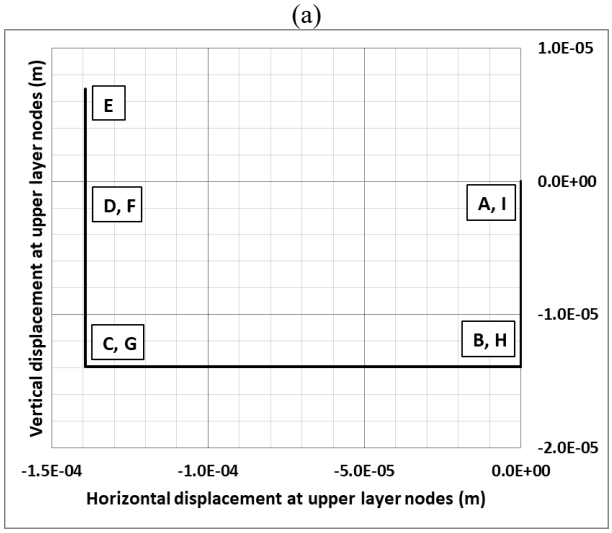

(b)

Fig. 1 Verification example description; (a) The 6-node interface element with fixed lower layer nodes and (b) Control displacements imposed at upper layer nodes

The nodes of the lower layer (1-3) are kept fixed, and specified displacements are imposed for the nodes of the upper layer (4-6) in horizontal and vertical directions. The applied control displacements paths are illustrated in Fig. 1(b).

It is noted that vertical downward displacements are imposed initially (Path A-B), then horizontal displacements are applied with vertical displacements being kept constant (Path B-C). Subsequently, upward vertical displacements are imposed while horizontal displacements are kept constant (Path C-D and D-E). Thereafter, the same path is reversed back to the initial position (Paths E-F, F-G, G-H and H-I).

The shear stress vs normal stress is depicted in Fig. 2 for one of the typical Gauss points, all behaving similarly. It is noted that during path A-B normal compressive stress gradually increases. For path B-C, shear stress gradually increases. However, it is limited by the yield surface. During path C-D, it moves on the yield surface till it

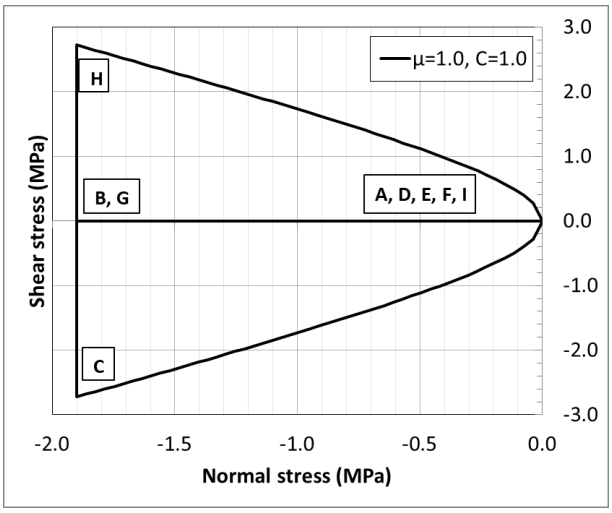

Fig. 2 The shear stress vs normal stress for one of the typical Gauss points ($c = 1.0$ MPa and $\mu = 1.0$)

reaches zero shear and normal stress. There is joint opening and subsequent closure for paths D-E and E-F. The stresses remain zero during these paths as expected. For path F-G, normal compressive stress is induced again. During path G-H, shear stress gradually increases in the other direction. However, it is limited by the yield surface once again. Finally, for path H-I, it moves on the yield surface till it reaches zero shear and normal stress at the end of the process.

5. Application on concrete gravity dams

In this section, the sliding behavior of Pine Flat gravity dam is being studied by application of the nonlinear joint-model discussed above. This dam is located near Fresno, California. It should be also mentioned that it was necessary to modify a special purpose finite element program (i.e., MAP-76, Lotfi (2009)) for this purpose based on the theories explained in sections 2 and 3. Moreover, it is worthwhile to emphasize that there are different advanced fluid-structure interaction alternatives that are developed in recent years. In particular, wavenumber approach (Lotfi and Samii 2012), high-order truncation conditions (Samii and Lotfi 2012, Lotfi and Lotfi 2021) and perfectly matched layers options (Khazaee and Lotfi 2014a, b).

Some of these options are augmented to the MAP-76 program. Of course, most researchers still prefer to utilize added mass approach to simplify the problem and avoid long execution times when they are dealing with different material or joint non-linearity in their analysis.

5.1 Modeling and basic properties

The finite element discretization of the tallest monolith of the dam on flexible foundation rock is illustrated in Fig. 3. The model consists of 40, 968 second order 8-noded isoparametric plane solid elements for dam body and foundation rock region, respectively. Moreover, 4 second order isoparametric interface elements (i.e., 6-noded) are utilized for modeling the dam-foundation rock interface. The plane stress and plane strain assumptions are utilized for dam body and foundation rock region, respectively. Moreover, concrete properties are taken as; modulus of elasticity (E_d) of 22.75 GPa, Poisson's ratio (ν_d) of 0.2, and unit weight (γ_d) of 24.8 kN/m3. Meanwhile, foundation rock properties are taken as; Poisson's ratio (ν_f) of 0.33, and unit weight (γ_f) of 26.4 kN/m3. Furthermore, three values of foundation rock elastic modulus were chosen ($E_f/E_d = \infty$, 1 and 0.25).

As for reservoir's water characteristics, the incompressible water assumption is utilized and its weight density (γ_w) is taken as 9.81 kN/m3. Moreover, dam-water interaction effects are included using the modified Westergaard added mass procedure (Westergaard 1933, Kuo 1982) and water height (h_w) is taken as 116.19 m.

5.2 Loading and solution procedure

The dam-foundation rock system is initially subjected to dam's self-weight, hydrostatic pressures and base uplift pressures. The latter loading is assumed to have a linear distribution varying from 40% of hydrostatic pressure (to account for drainage) at the heel of the dam to zero at the toe. The static loadings are applied gradually at the negative range of time which excludes inertia and damping effects in this process. Dynamic loading commences at time zero, and it includes 20 sec of the Taft record, S69E component scaled to a peak acceleration of 0.4 g which is applied in the horizontal direction.

The analyses are carried out in time domain using HHT-α algorithm with a time step $\Delta t = 0.01$ sec and $\alpha = 0.3$. Furthermore, Rayleigh damping is utilized in the analyses and its coefficients are determined such that the damping ratios for the first and third modes of vibration become 5% of the critical damping.

5.3 Results

In the initial stage, three linear analyses (i.e., cases P0,

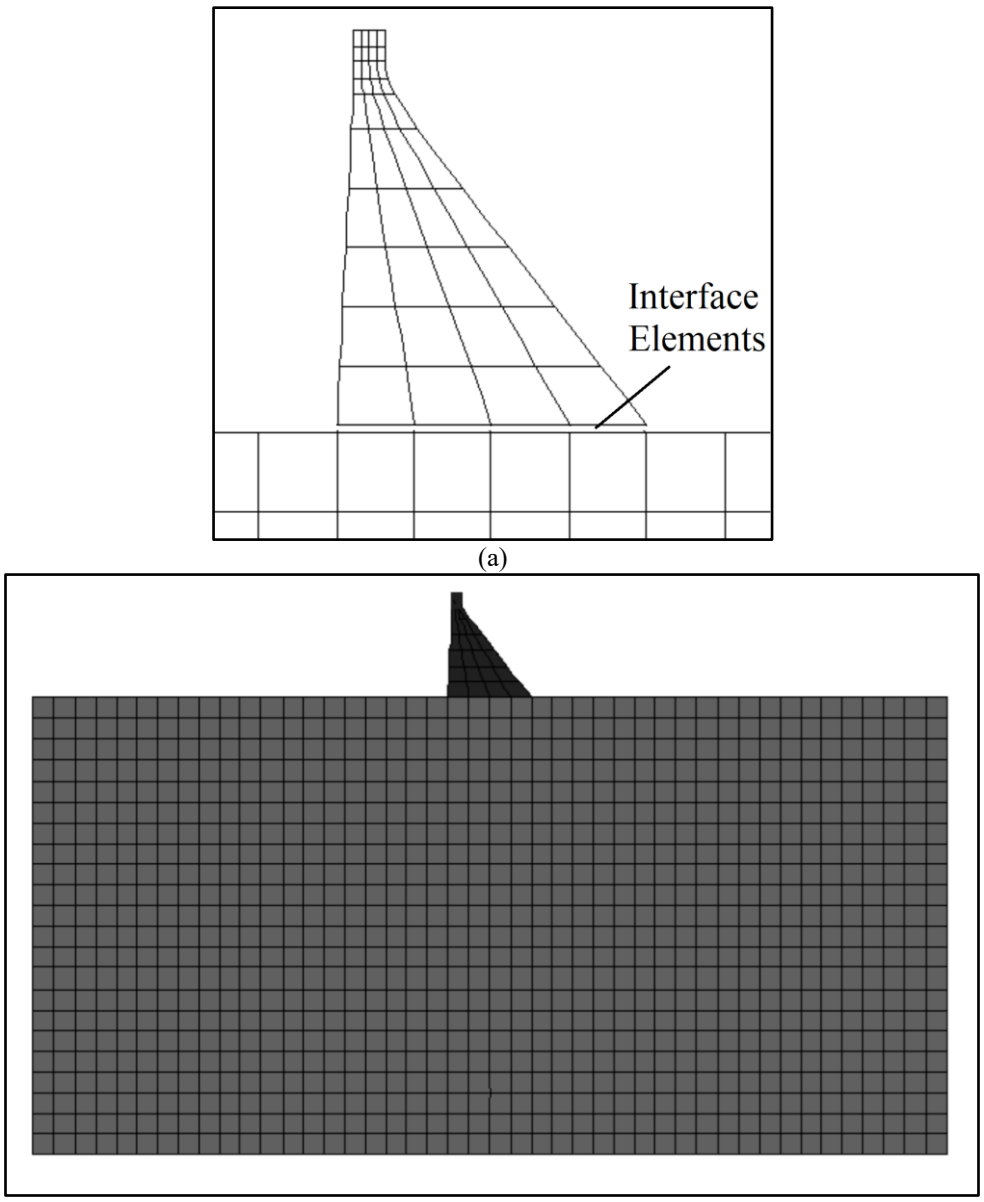

Fig. 3 The finite element mesh of Pine Flat Gravity dam-foundation rock system; (a) Close up view and (b) Complete mesh

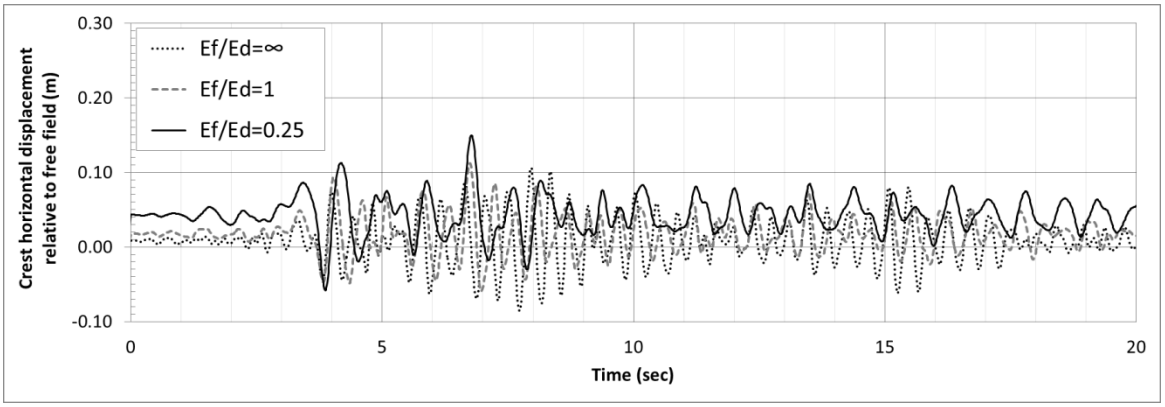

Fig. 4 History of crest horizontal displacement relative to free field for linear cases (P0, P10, P20)

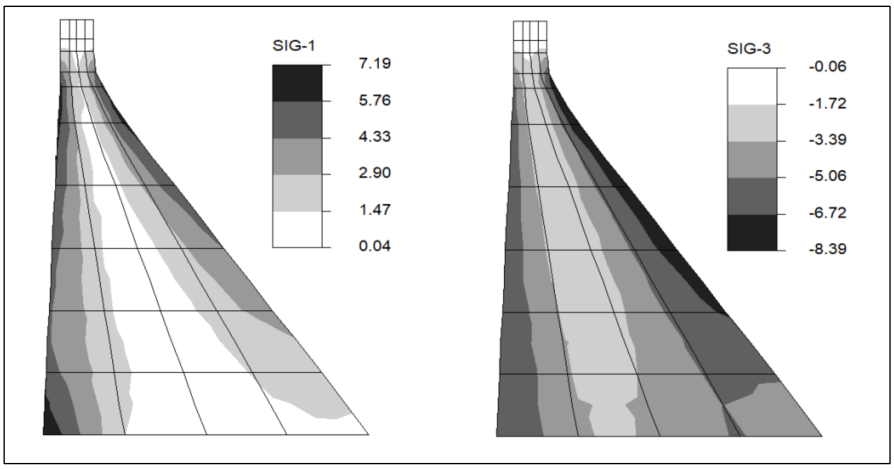

(a) $\left(\boldsymbol{E_f/E_d = \infty}\right)$

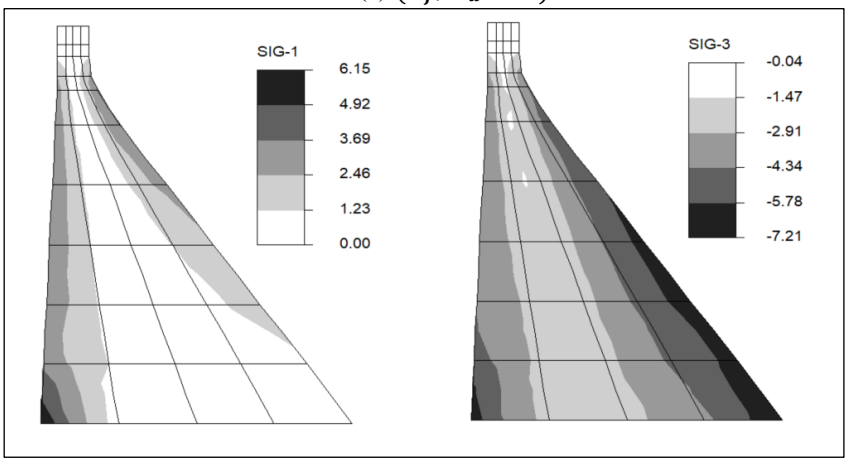

(b) $\left(\boldsymbol{E_f/E_d = 1}\right)$

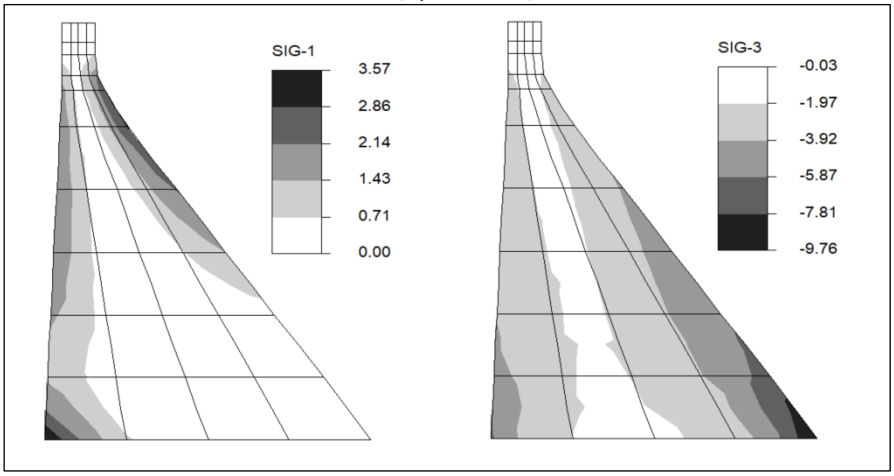

(c) $\left(\boldsymbol{E_f/E_d = 0.25}\right)$

Fig. 5 Envelope of first and third principal stresses for linear cases; (a) P0, (b) P10 and (c) P20

P10, P20 corresponding to $E_f/E_d = \infty$, 1 and 0.25) are carried out which can be used as basis for subsequent nonlinear analyses. The histories of dam crest horizontal displacements are illustrated in Fig. 4 for these cases. It is observed that minimum and maximum displacements are (-0.086, -0.059, -0.058 m), (0.106, 0.112, 0.150 m) for these three cases, respectively. Moreover, the envelopes of first and third principal stresses (i.e., σ_1 and σ_3) throughout dam body are depicted in Fig. 5. It is noted that maximum tensile stress occurs at dam's heel and it reaches a high value of 7.19 MPa for P0 (rigid foundation case). Of course, this high value decreases as E_f/E_d ratio decreases. It becomes 6.15, 3.57 MPa for the other two cases (P10, P20). Furthermore, the maximum compressive stress (-8.39 MPa) is induced at mid-height at D/S face of the dam for P0 (rigid foundation case). This value decreases for P10 (-7.21 MPa) and increases for P20 (-9.76 MPa). It is also observed that location of maximum compressive stress lowers down from

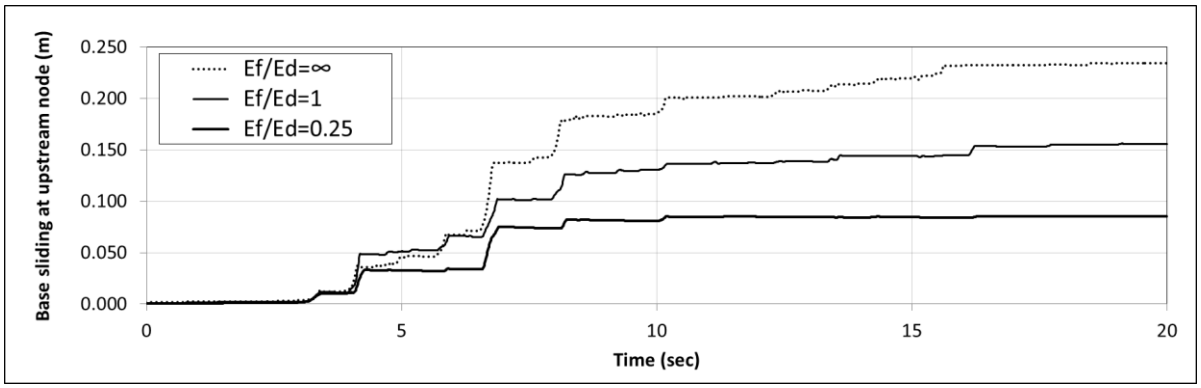

(a) **(μ =0.8 and c =0.0)**

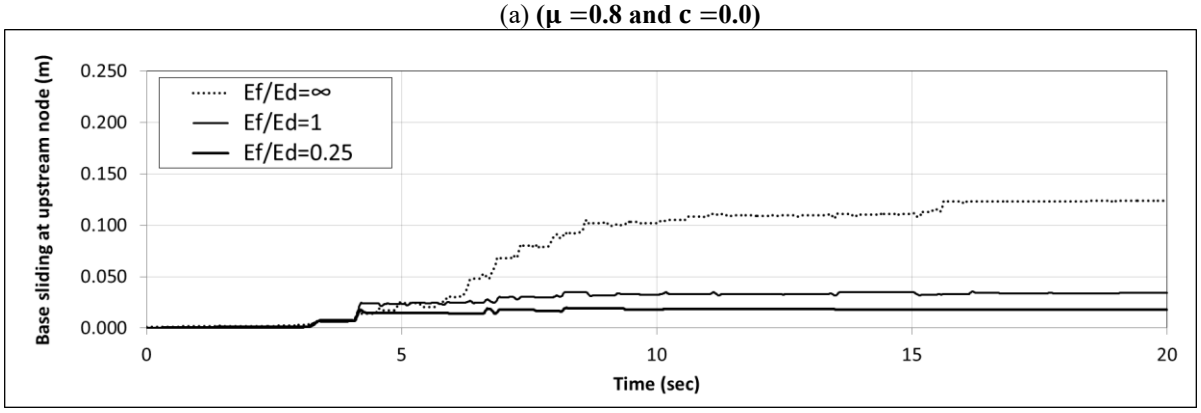

(b) **(μ =1.0 and c =0.2)**

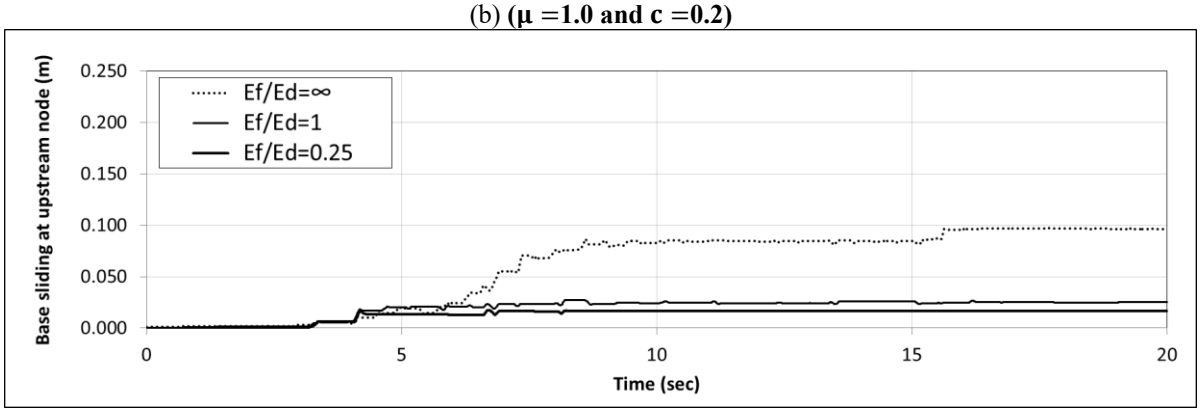

(c) **(μ =1.2 and c =0.4)**

Fig. 6 History of base sliding for U/S base node of nonlinear cases; (a) P1, P11, P21, (b) P5, P15, P25 and (c) P9, P19, P29

mid-height at D/S face to dam's toe as E_f/E_d ratio decreases.

Thereafter, a parameter study is carried out to evaluate the influence of friction coefficient (μ) and cohesion (c) on earthquake response of Pine Flat dam. It should be emphasized that these parameters are actually the apparent friction coefficient and apparent cohesion. This is due to the fact a hyperbolic yield surface is utilized in the model rather than a Mohr-Coulomb type. For this aim, 27 nonlinear cases are considered (P1-P9, P11-P19, P21-P29) as listed in Table 1.

It is noticed that in particular, three values of apparent friction coefficient (i.e., $\mu = 0.8$, 1.0 and 1.2) are considered and for each of these, the apparent cohesion are varied as $c = 0.0$, 0.2 and 0.4 which results in a total of nine cases to investigate the effects of these two parameters under three different foundation rock conditions ($E_f/E_d = \infty$, 1 and 0.25). As mentioned, three linear cases discussed above, were also considered to provide the initial basis responses for nonlinear comparison purposes.

The results for nonlinear cases are presented in Figs. 6-12 which are discussed in the remaining portion of this section. These results consist of history of base sliding for U/S base node (Fig. 6), history of joint opening at U/S base node (Fig. 7), history of crest horizontal displacement relative to free field (Fig. 8), and history of crest horizontal displacement relative to the base U/S node (Fig. 9).

Additionally, envelopes of first and third principal stresses through time are provided in Figs. 10-12 for different cases. Moreover, the maximum values of responses are summarized in Tables 2 and 3 below. It should be emphasized that although these Tables covers the summary of all 30 cases (3 linear cases and 27 nonlinear cases) such that one can follow the global trend, the Figs. 6-

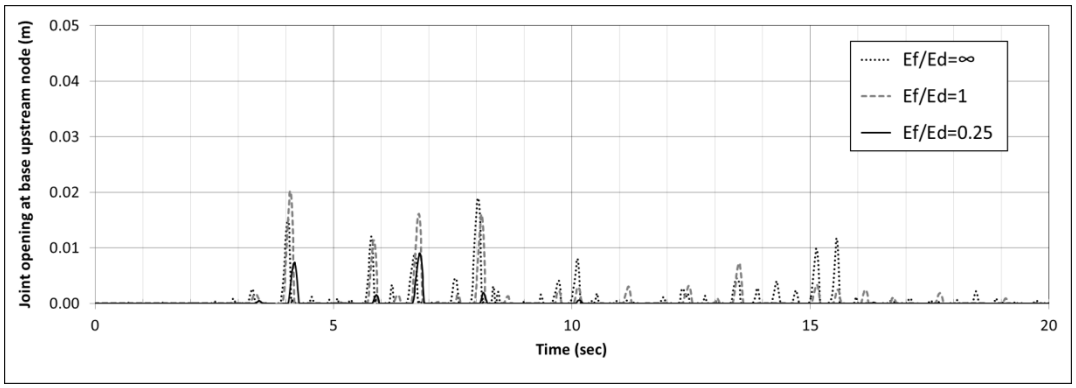

(a) **(μ =0.8 and c =0.0)**

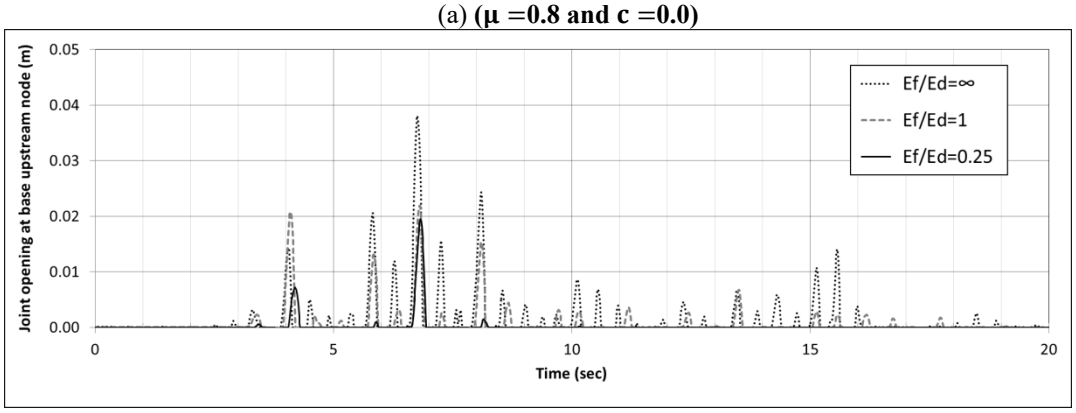

(b) **(μ =1.0 and c =0.2)**

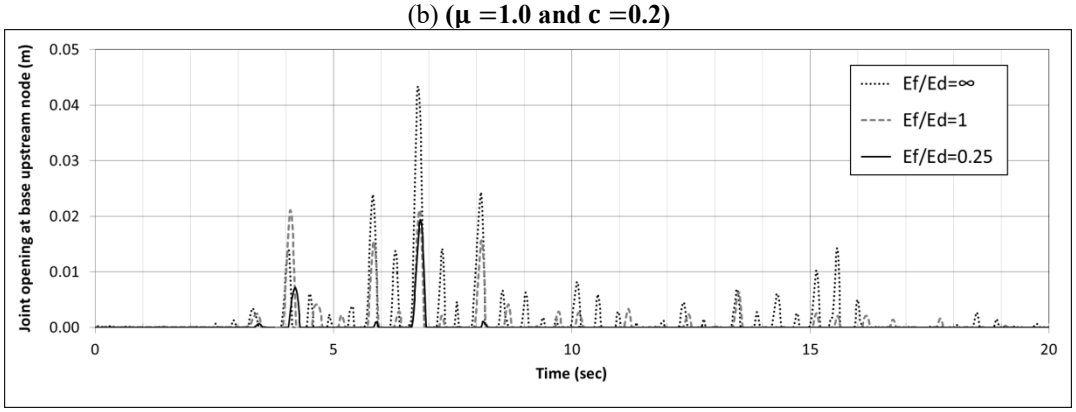

(c) **(μ =1.2 and c =0.4)**

Fig. 7 History of joint opening for U/S base node of nonlinear cases; (a) P1, P11, P21, (b) P5, P15, P25 and (c) P9, P19, P29

Table 1 Symbolic names and main parameters of considered cases

Analysis	E_f/E_d			Apparent friction coefficient (μ)	Apparent cohesion (c)
	∞	1.0	0.25		
Linear	P0	P10	P20	---	---
Nonlinear	P1	P11	P21	0.8	0.0
	P2	P12	P22	0.8	0.2
	P3	P13	P23	0.8	0.4
	P4	P14	P24	1.0	0.0
	P5	P15	P25	1.0	0.2
	P6	P16	P26	1.0	0.4
	P7	P17	P27	1.2	0.0
	P8	P18	P28	1.2	0.2
	P9	P19	P29	1.2	0.4

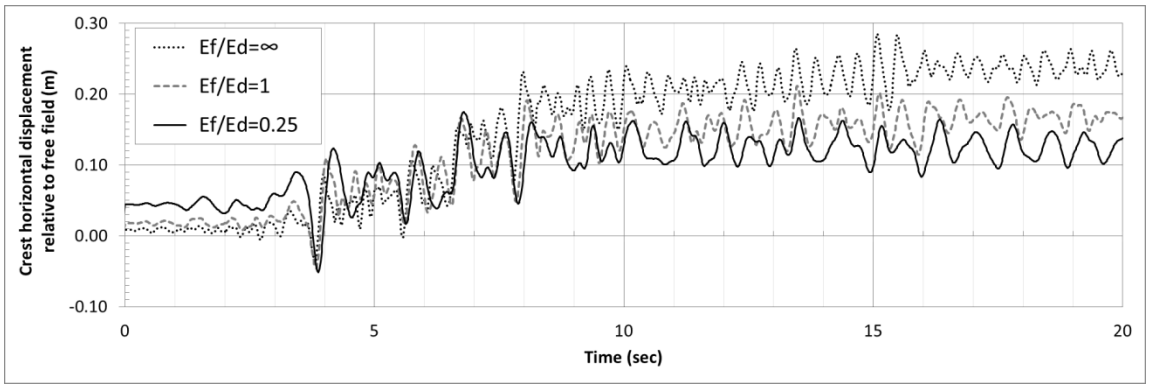

(a) **(μ =0.8 and c =0.0)**

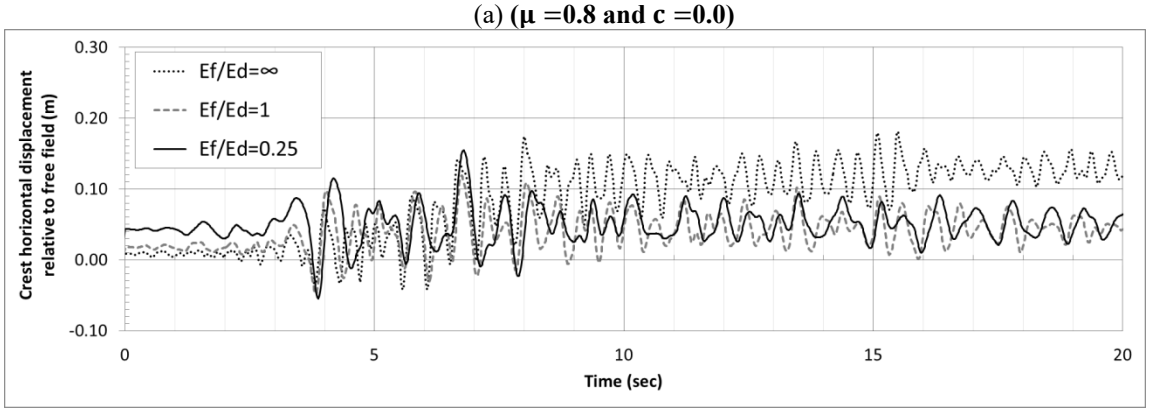

(b) **(μ =1.0 and c =0.2)**

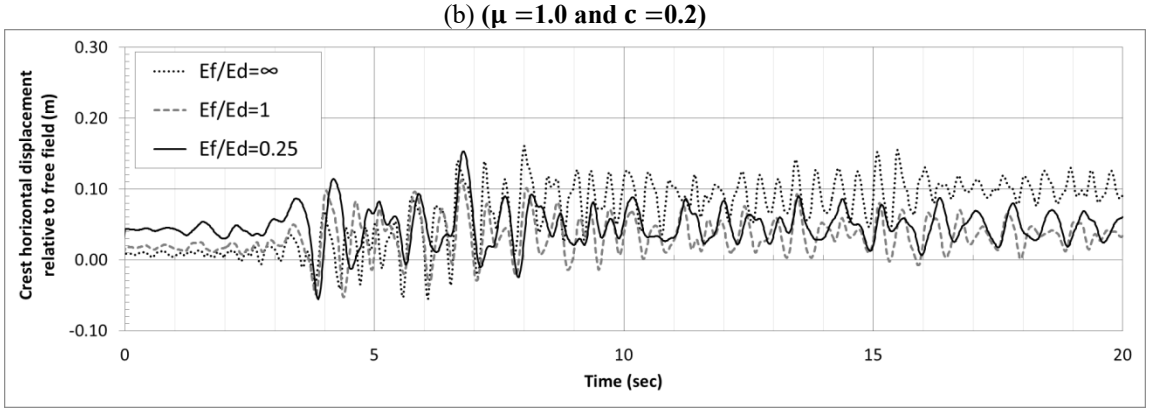

(c) **(μ = 1.2 and c =0.4)**

Fig. 8 History of crest horizontal displacement relative to free field for nonlinear cases; (a) P1, P11, P21, (b) P5, P15, P25 and (c) P9, P19, P29

12 are mainly concentrated on three groups of cases (total of 9 prominent cases). In particular, these groups correspond to cases with low ($\mu = 0.8$ and $c = 0.0$), moderate ($\mu = 1.0$ and $c = 0.2$), and high ($\mu = 1.2$ and $c = 0.4$) considered joint properties. Moreover, each group comprised of three different foundation rock condition cases ($E_f/E_d = \infty$, 1 and 0.25). Therefore, these three groups correspond to (P1, P11, P21), (P5, P15, P25), (P9, P19, P29) cases, respectively. It is apparent that this strategy in presentation of results is mainly due to lack of space.

Let us first concentrate on history of base sliding for U/S base node (Fig. 6) and its values at the end of analyses which are presented in Table 2. It is noted that for low joint properties group (i.e., $\mu = 0.8$ and $c = 0.0$), maximum sliding (0.234 m) occurs for rigid foundation case (P1 case). This is also the highest value among all 27 considered nonlinear cases. Furthermore, it is noted that base sliding decreases as E_f/E_d ratio reduce for other cases of this group (0.156, 0.085 m for P11 and P21 cases, respectively). Similar trends are noted for different cases of the other two groups (moderate and high joint properties). In general, it can be asserted that joint sliding decreases as joint properties increase, and E_f/E_d ratio reduces. Therefore, lowest joint sliding is 0.016 m which corresponds to P29 case (i.e., $\mu = 1.2$, $c = 0.4$ and $E_f/E_d = 0.25$). It should be mentioned that base sliding for D/S node are also reported for different cases in Table 2. It is noticed that in general, they are slightly lower than the corresponding values at U/S node. For this reason, their histories are not presented due to space limitations.

Subsequently, the history of joint opening at U/S node, are compared for those three joint properties groups in Fig.

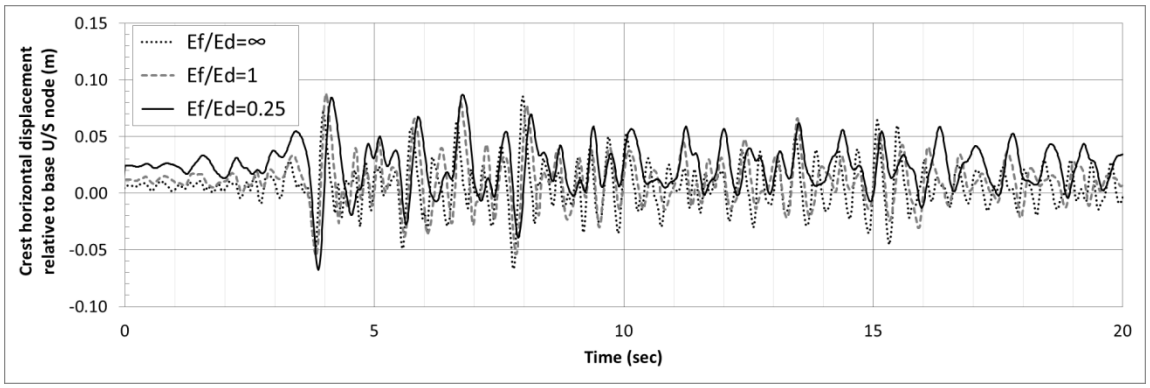

(a) **(μ =0.8 and c =0.0)**

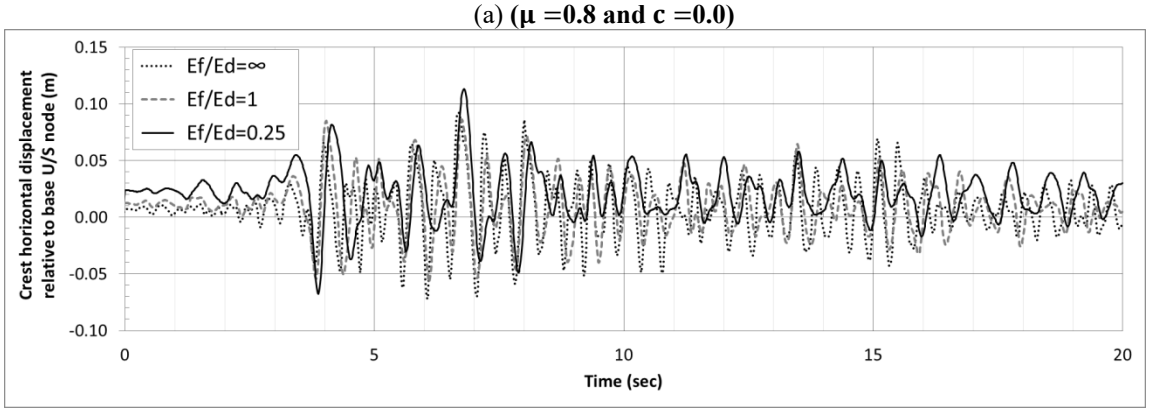

(b) **(μ =1.0 and c =0.2)**

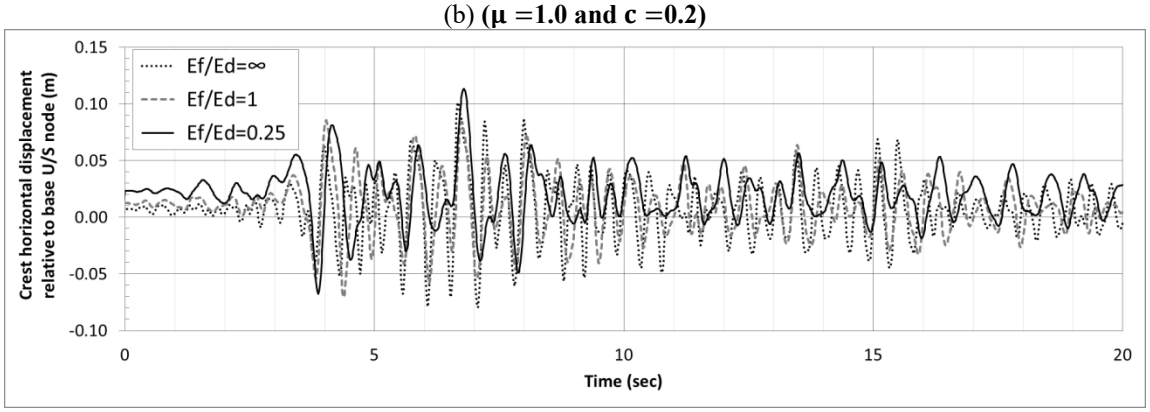

(c) **(μ = 1.2 and c =0.4)**

Fig. 9 History of crest horizontal displacement relative to base U/S node for nonlinear cases; (a) P1, P11, P21, (b) P5, P15, P25 and (c) P9, P19, P29

7, and their maximum values are summarized in Table 2.

It is observed that maximum joint opening at U/S node is greatest for P9 case (0.043 m) which corresponds to high joint properties and rigid foundation case (i.e., $\mu = 1.2$, $c = 0.4$ and $E_f/E_d = \infty$). It is also noted by checking Table 2 that maximum joint opening at U/S node for rigid foundation cases, increases as apparent friction coefficient and apparent cohesion values become larger. However, it is almost constant (range of 0.019-0.022 m) for different cases corresponding to $E_f/E_d = 1$ and 0.25 (with the exception of P21 case).

Thereafter, history of crest horizontal displacement relative to free field, are presented for three mentioned groups in Fig. 8 and their minimum, maximum values are listed for all cases in Table 2.

Based on Fig. 8, it is observed that the highest amount for maximum crest horizontal displacement (relative to free field) value (0.285 m) occurs for rigid foundation condition and low joint properties (i.e., $\mu = 0.8$ and $c = 0.0$). This is also the maximum value occurred among all 27 nonlinear cases according to Table 2. Moreover, it is observed that maximum crest horizontal displacement relative to free field values are in general much higher for nonlinear cases than corresponding results noted for linear cases (Fig. 4 and Table 2). Obviously, this is as a result of base sliding occurring in nonlinear cases.

Similarly, history of crest horizontal displacement relative to base, are also presented for three mentioned groups in Fig. 9 and their minimum, maximum values are provided in Table 2. It is noticed that there is not much difference between these maximum values due to the fact

Table 2 Maximum responses for different cases

E_f/E_d	Case	μ	c	Base sliding (m)		Joint opening at U/S node (m)	Crest Hor. Displ. (relative to free field)		Crest Hor. Displ. (relative to base)	
				U/S	D/S		Min	Max	Min	Max
∞	P0	---	---	---	---	---	-0.086	0.106	-0.086	0.106
	P1	0.8	0.0	0.234	0.230	0.019	-0.038	0.285	-0.067	0.086
	P2	1.0	0.0	0.145	0.140	0.033	-0.034	0.200	-0.063	0.088
	P3	1.2	0.0	0.120	0.116	0.042	-0.047	0.177	-0.080	0.096
	P4	0.8	0.2	0.176	0.170	0.024	-0.036	0.232	-0.082	0.094
	P5	1.0	0.2	0.124	0.119	0.038	-0.042	0.181	-0.072	0.092
	P6	1.2	0.2	0.102	0.098	0.043	-0.052	0.161	-0.083	0.099
	P7	0.8	0.4	0.135	0.130	0.029	-0.036	0.193	-0.073	0.090
	P8	1.0	0.4	0.107	0.102	0.042	-0.050	0.167	-0.076	0.097
	P9	1.2	0.4	0.097	0.092	0.043	-0.055	0.161	-0.080	0.101
1.0	P10	---	---	---	---	---	-0.059	0.112	-0.062	0.102
	P11	0.8	0.0	0.156	0.151	0.020	-0.046	0.211	-0.055	0.088
	P12	1.0	0.0	0.053	0.045	0.022	-0.048	0.131	-0.056	0.088
	P13	1.2	0.0	0.035	0.026	0.022	-0.048	0.117	-0.065	0.086
	P14	0.8	0.2	0.066	0.059	0.022	-0.048	0.139	-0.054	0.087
	P15	1.0	0.2	0.034	0.025	0.022	-0.048	0.119	-0.057	0.086
	P16	1.2	0.2	0.028	0.018	0.021	-0.050	0.114	-0.069	0.085
	P17	0.8	0.4	0.043	0.034	0.022	-0.048	0.126	-0.056	0.087
	P18	1.0	0.4	0.028	0.018	0.022	-0.048	0.115	-0.058	0.086
	P19	1.2	0.4	0.025	0.015	0.021	-0.053	0.112	-0.070	0.085
0.25	P20	---	---	---	---	---	-0.058	0.150	-0.066	0.116
	P21	0.8	0.0	0.085	0.083	0.009	-0.052	0.175	-0.068	0.087
	P22	1.0	0.0	0.025	0.016	0.019	-0.055	0.158	-0.068	0.111
	P23	1.2	0.0	0.017	0.000	0.019	-0.055	0.154	-0.068	0.113
	P24	0.8	0.2	0.029	0.022	0.019	-0.053	0.161	-0.067	0.110
	P25	1.0	0.2	0.018	0.005	0.019	-0.055	0.154	-0.068	0.113
	P26	1.2	0.2	0.017	0.000	0.019	-0.056	0.153	-0.068	0.113
	P27	0.8	0.4	0.020	0.010	0.020	-0.054	0.157	-0.067	0.114
	P28	1.0	0.4	0.017	0.002	0.019	-0.055	0.154	-0.068	0.113
	P29	1.2	0.4	0.016	0.000	0.019	-0.056	0.153	-0.068	0.113

Table 3 Maximum stresses for different cases

μ	c	E_f/E_d								
		∞			1.0			0.25		
		Case	σ_1^{max} (MPa)	σ_3^{min} (MPa)	Case	σ_1^{max} (MPa)	σ_3^{min} (MPa)	Case	σ_1^{max} (MPa)	σ_3^{min} (MPa)
---	---	P0	7.19	-8.39	P10	6.15	-7.21	P20	3.57	-9.76
0.8	0.0	P1	6.65	-7.06	P11	5.62	-7.22	P21	2.88	-7.69
1.0	0.0	P2	7.99	-11.19	P12	4.16	-9.32	P22	2.92	-9.61
1.2	0.0	P3	8.47	-12.91	P13	4.34	-10.74	P23	2.91	-10.43
0.8	0.2	P4	7.53	-7.95	P14	3.83	-7.94	P24	2.91	-8.77
1.0	0.2	P5	8.02	-11.27	P15	4.10	-9.45	P25	2.90	-9.89
1.2	0.2	P6	8.44	-11.84	P16	4.70	-11.14	P26	2.90	-10.46
0.8	0.4	P7	7.49	-8.71	P17	4.07	-8.17	P27	2.91	-8.95
1.0	0.4	P8	8.22	-11.27	P18	4.30	-9.80	P28	2.90	-10.04
1.2	0.4	P9	8.57	-11.19	P19	4.78	-10.84	P29	2.90	-10.51

that horizontal base sliding is not contributing anything to these values. However, in general the dominant period seem to increase as E_f/E_d ratio decreases (i.e., foundation rock becomes more flexible).

As mentioned, envelope of first and third principal stresses, are presented in Figs. 10-12 for the three mentioned groups and their maximum values are summarized in Table 3. It is observed that highest amount of tensile stresses ($\sigma_1^{max} = 8.57$ MPa) occurs for case P9, rigid foundation condition and when apparent friction coefficient, cohesion have their largest considered values (i.e., $\mu = 1.2$ and $c = 0.4$). This is not the case for

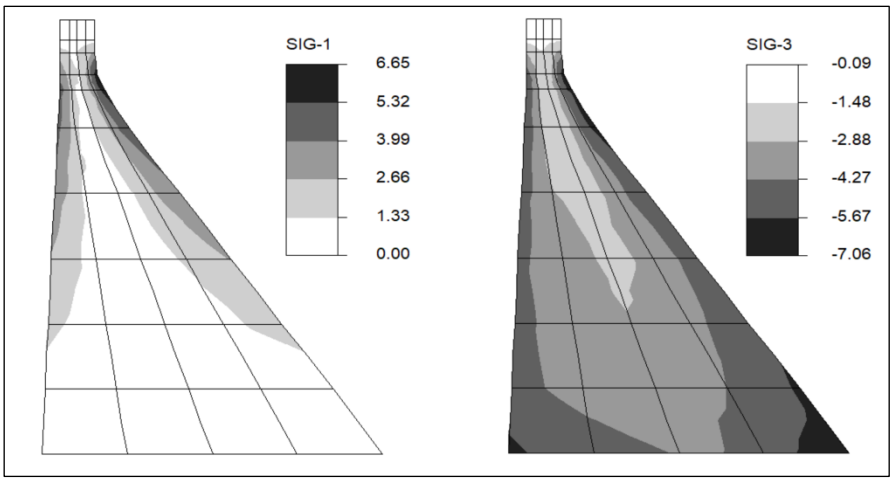

(a) $\left(\boldsymbol{E_f/E_d = \infty}\right)$

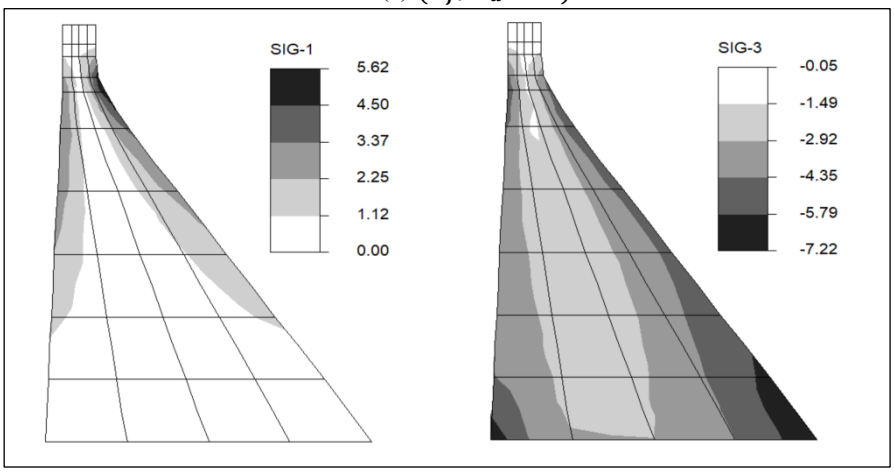

(b) $\left(\boldsymbol{E_f/E_d = 1}\right)$

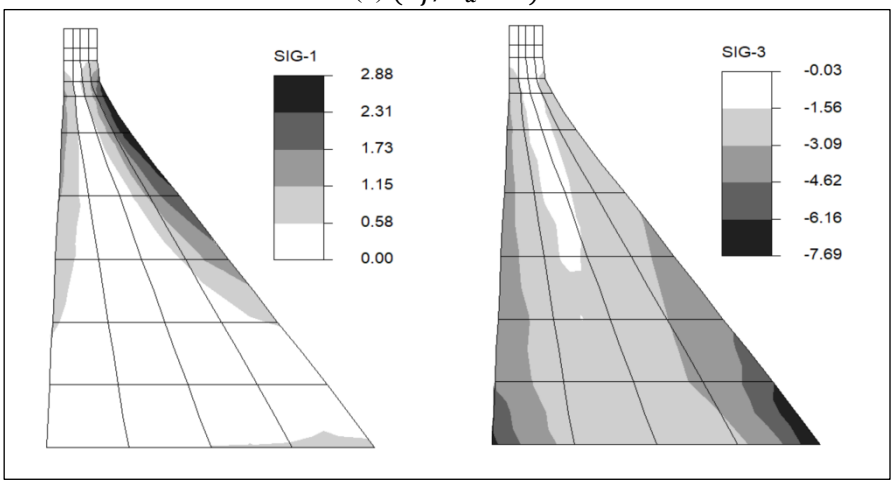

(c) $\left(\boldsymbol{E_f/E_d = 0.25}\right)$

Fig. 10 Envelope of first and third principal stresses for nonlinear cases (μ =0.8 and c =0.0); (a) P1, (b) P11 and (c) P21

maximum compressive stress ($\sigma_3^{\min} = -12.91$ MPa) which occurs for the case of $\mu = 1.2$ and $c = 0.0$. It is also worthwhile to mention that for these nonlinear cases, the maximum value of tensile stresses in the dam body occurs near the kink of the D/S face at the top portion of the dam. This is contrary to the corresponding linear cases (Fig. 5) which it is noticed that maximum tensile stresses occur at dam heel. Moreover, it should be mentioned that for nonlinear cases, the maximum value of compressive stresses in the dam body occur at the dam toe, contrary to the corresponding linear cases (Fig. 5) which it is noticed that maximum compressive stress may occur at dam mid-height on D/S face in certain cases ($E_f/E_d = \infty$, case P0). This change in behavior is mainly due to joint opening at

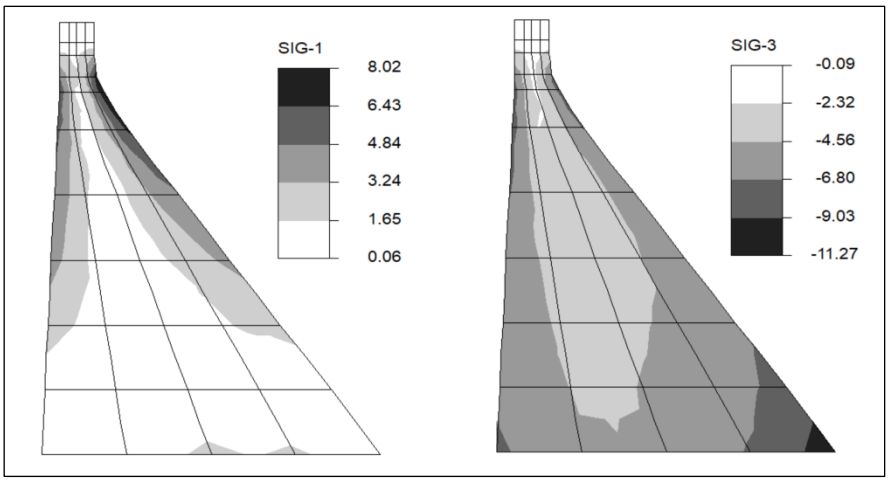

(a) $\left(\boldsymbol{E_f/E_d = \infty}\right)$

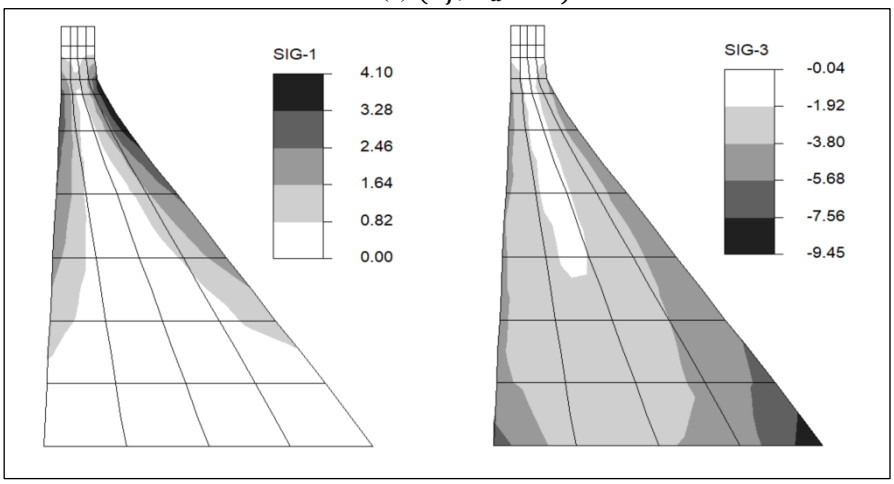

(b) $\left(\boldsymbol{E_f/E_d = 1}\right)$

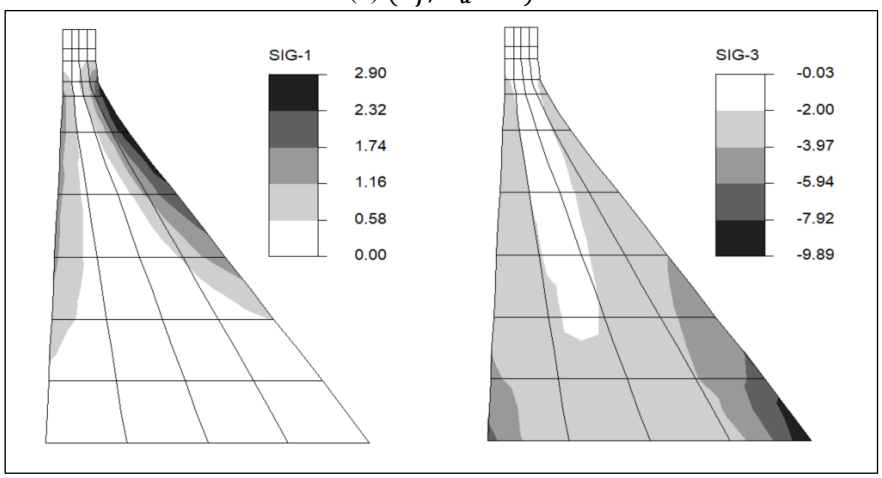

(c) $\left(\boldsymbol{E_f/E_d = 0.25}\right)$

Fig. 11 Envelope of first and third principal stresses for nonlinear cases μ =1.0 and c = 0.2); (a) P5, (b) P15 and (c) P25

dam heel which releases high tensile stresses at that location and result in high compressive stresses at dam toe for nonlinear cases.

In general, it can also be asserted that for all three mentioned joint properties groups (Figs. 10-12), the maximum tensile stresses are highest for rigid foundation condition and it decreases as E_f/E_d ratio reduces. This is mainly as a result of radiation damping effects.

6. Conclusions

In the present study, a simplified non-associated joint model was employed. The formulation and its theoretical concepts were discussed. Then, an initial verification of the model was considered to control its implementation and to show its characteristics. The model for this example relates to a single 6-node isoparametric interface element under a

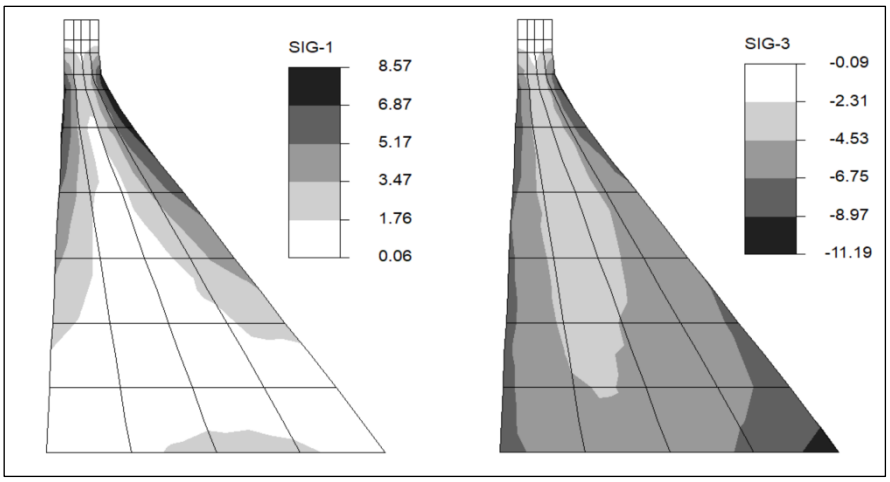

(a) $\left(\boldsymbol{E_f/E_d = \infty}\right)$

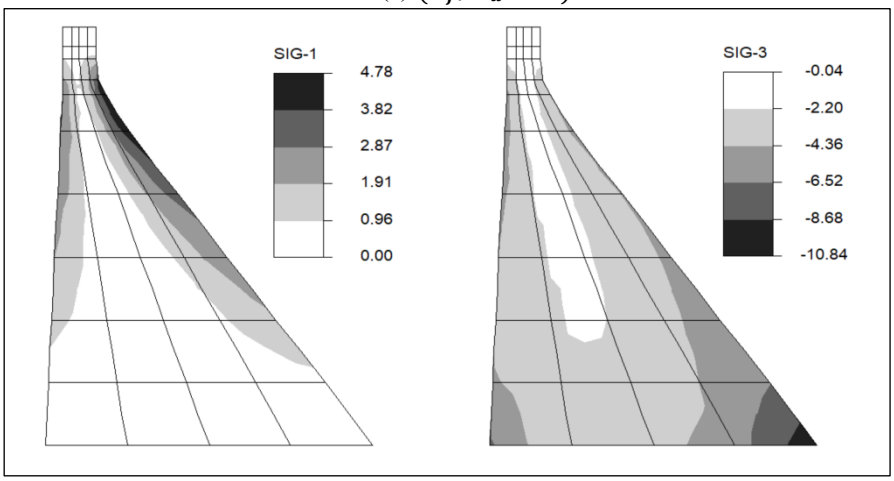

(b) $\left(\boldsymbol{E_f/E_d = 1}\right)$

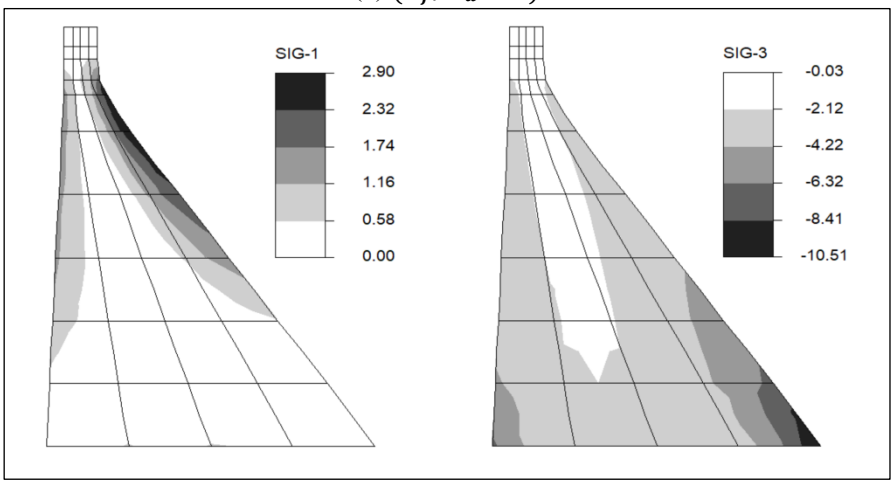

(c) $\left(\boldsymbol{E_f/E_d = 0.25}\right)$

Fig. 12 Envelope of first and third principal stresses for nonlinear cases (μ =1.2 and c =0.4); (a) P9, (b) P19 and (c) P29

certain control displacement conditions.

Thereafter, the sliding behavior of Pine Flat gravity dam was studied by application of the nonlinear joint-model discussed above. In particular, a parameter study is carried out to evaluate the influence of apparent friction coefficient (μ) and apparent cohesion (c) on earthquake response of Pine Flat gravity dam for three different foundation rock conditions ($E_f/E_d = \infty$, 1 and 0.25). Overall, the main conclusions obtained from this study can be summarized as follows:

- In general, it can be asserted that joint sliding decreases as joint properties (apparent friction coefficient and apparent cohesion) increases, and E_f/E_d ratio reduces.

- It is noted that maximum joint opening at U/S node for rigid foundation cases, increases as apparent friction coefficient and apparent cohesion values become larger. However, it is almost constant for different cases corresponding to $E_f/E_d = 1$ and 0.25 (with the exception of P21 case).
- It is observed that maximum crest horizontal displacement relative to free field values are in general much higher for nonlinear cases than corresponding results noted for linear cases regardless of the value of E_f/E_d ratio. Obviously, this is as a result of base sliding occurring in nonlinear cases.
- In regard to crest horizontal displacement relative to base, it is noticed that there is not much difference between the maximum values for different cases due to the fact that horizontal base sliding is not contributing anything to these values. However, in general the dominant period seem to increase as E_f/E_d ratio decreases (i.e., foundation rock becomes more flexible).
- It is observed that highest amount of tensile stresses occurs for rigid foundation condition and when apparent friction coefficient, cohesion have their largest considered values (i.e., $\mu = 1.2$ and $c = 0.4$). Moreover, in general for nonlinear cases, the maximum value of tensile stresses in the dam body occurs near the kink of the D/S face at the top portion of the dam, contrary to the corresponding linear cases which it is noticed that maximum tensile stresses occur at dam heel.
- For nonlinear cases, the maximum value of compressive stresses in the dam body occur at the dam toe, contrary to the corresponding linear cases which it is noticed that maximum compressive stress may occur at dam mid-height on D/S face in certain cases ($E_f/E_d = \infty$, case P0). This change in behavior is mainly due to joint opening at dam heel which releases high tensile stresses at that location and result in high compressive stresses at dam toe for nonlinear cases.
- In general, it can also be asserted that for all three mentioned joint properties groups, the maximum tensile stresses are highest for rigid foundation condition and it decreases as E_f/E_d ratio reduces. This is mainly as a result of radiation damping effects.

References

Ahmadi, M.T. and Razavi, S. (1992), "A three-dimensional joint opening analysis of an arch dam", *Comput. Struct.*, **44**(1-2), 187-192. https://doi.org/10.1016/0045-7949(92)90237-T.

Ahmadi, M.T., Izadinia, M. and Bachmann, H. (2001), "A discrete crack joint model for nonlinear dynamic analysis of concrete arch dams", *Comput. Struct.*, **79**(4), 403-420. https://doi.org/10.1016/S0045-7949(00)00148-6.

Akbari, R. and Lotfi, V. (2022), "Nonlinear dynamic analysis of concrete gravity dams utilizing a simplified continuum damage model and different damping algorithms", *Asian J. Civil Eng.*, **24**(2), 453-468. https://doi.org/10.1007/s42107-022-00511-2.

Arabshahi, H.R. and Lotfi, V. (2008), "Earthquake response of concrete gravity dams including dam–foundation interface nonlinearities", *Eng. Struct.*, **30**(11), 3065-3073. https://doi.org/10.1016/j.engstruct. 2008.04.018.

Arabshahi, H.R. and Lotfi, V. (2009), "Nonlinear dynamic analysis of arch dams with joint sliding mechanism", *Eng. Comput.*, **26**(5), 464-482. https://doi.org/10.1108/02644400910970158.

Azmi, M. and Paultre, P. (2002), "Three-dimensional analysis of concrete dams including contraction joint non-linearity", *Eng. Struct.*, **24**(5), 757-771. https://doi.org/10.1016/S0141-0296(02)00005-6.

Basu, U. and Chopra, A.K. (2003), "Perfectly matched layers for time-harmonic elastodynamics of unbounded domains: Theory and finite-element implementation", *Comput. Method. Appl. M., Eng.*, **192**(11-12), 1337-1375. https://doi.org/10.1016/S0045-7825(02)00642-4.

Chaves, J.W. and Fenves, G.L. (1993), "Earthquake analysis and response of concrete gravity dams including base sliding", Report no. UCB/EERC-93/07. Berkeley (CA): University of California at Berkeley.

Chen, D.H., Yang, Z.H., Wang, M. and Xie, J.H. (2019), "Seismic performance and failure modes of the Jin'anqiao concrete gravity dam based on incremental dynamic analysis", *Eng. Fail. Anal.*, **100**(6), 227-244. https://doi.org/10.1016/j.engfailanal.2019.02.018.

Dehghanmarvastya, S. and Lotfi, V. (2023a), "Dynamic analysis of Pine Flat dam-reservoir system utilizing Hagstrom-Warburton truncation boundary condition", *Coupled Syst. Mech.*, **12**(4), 365-389. https://doi.org/10.12989/csm.2023.12.4.365.

Dehghanmarvastya, S. and Lotfi, V. (2023b), "Application of G-N high-order boundary condition on time harmonic analysis of concrete gravity dam-reservoir systems", *Eng. Comput.*, **40**(2), 313-334. https://doi.org/10.1108/EC-06-2022-0401.

Fenves, G.L., Mojtahedi, S. and Reimer, R.B. (1989) "ADAP-88: A computer program for nonlinear earthquake analysis of concrete arch dams", Report No. UCB/EERC 89/12, Earthquake Engineering Research Center, College of Engineering, University of California at Berkeley, USA.

Fenves, G.L., Mojtahedi, S. and Reimer, R.B. (1992), "Effects of contraction joints on earthquake response of an arch dam", *J. Struct. Eng. - ASCE*, **118**(4), 1039-1055. https://doi.org/10.1061/(ASCE)0733-9445(1992)118:4(1039).

Ghaboussi, J., Wilson, E.L. and Isenberg, J. (1973), "Finite element for rock joints and interfaces", *J. Soil Mech. Found. Division*, **99**(10), https://doi.org/10.1061/JSFEAQ.0001936.

Hall, J.F., Dowling, M.J. and El-Aidi, B. (1991), Defensive design of concrete gravity dams. Report no. EERL 91-02. Pasadena (CA): California Institute of Technology.

Hohberg, J.M. (1991), "Seismic arch dam analysis with full joint nonlinearity", *Proceedings of the Int. Conference on Dam Fracture*, Denver, Colorado.

Hohberg, J.M. (1992), "A joint element for the nonlinear dynamic analysis of arch dams", PhD Thesis and Report No. 186, Institute of Structural Engineering, ETH Zurich, Switzerland.

Hu, H. and Huang, Y. (2019), "A dynamic reliability approach to seismic vulnerability analysis of earth dams", *Geomech. Eng.*, **18**(6), 661-668, https://doi.org/10.12989/gae.2019.18.6.661.

Kamalzare, M., Marquez, H. and Zapata, O. (2022), "Seismic evaluation of Southern California embankment dam systems using finite element modeling", *Geomech. Eng.*, **31**(3), 319-328. https://doi.org/10.12989/gae.2022.31.3.319.

Karabulut, M. and Geniş, M. (2019), "Pseudo seismic and static stability analysis of the Torul Dam", *Geomech. Eng.*, **17**(2), 207-214. https://doi.org/10.12989/gae.2019.17.2.207.

Karalar, M. and Cavusli, M. (2021), "Three dimensional seismic deformation-shear strain-swelling performance of America-California Oroville Earth-Fill Dam", *Geomech. Eng.*, **24**(5), 443-456. https://doi.org/10.12989/gae.2021.24.5.443.

Khazaee, A. and Lotfi, V. (2014a), "Application of perfectly matched layers in the transient analysis of dam-reservoir systems", *J. Soil Dyn. Earthq. Eng.*, **60**(1), https://doi.org/10.1016/j.soildyn.2014.01.005.

Khazaee, A. and Lotfi, V. (2014b), "Time harmonic analysis of dam-foundation systems by perfectly matched layers", *Struct. Eng. Mech.*, **50**(3), https://doi.org/10.12989/sem.2014.50.3.349.

Kuo, J.S.H. (1982), "Fluid–structure interaction added mass computations for incompressible fluid", Report No. UCB/EERC 82/09, Earthquake Engineering Research Center, College of Engineering, University of California, Berkeley, USA.

Lau, D.T., Noruziaan, B. and Razaqpur, A.G. (1998), "Modeling of contraction joint and shear effects on earthquake response of arch dams", *Earthq. Eng. Struct. D.*, **27**(10), 1013-1029.

Lee, J. (1996), "Theory and implementation of plastic-damage model for concrete structures under cyclic and dynamic loading", PhD dissertation, Department of Civil and Environmental Eng., University of California, Berkeley, California.

Lee, J. and Fenves, G.L. (1998), "Plastic damage model for cyclic loading of concrete structures", *J. Eng. Mech. - ASCE*, **124**(8), 892-900. https://doi.org/10.1061/(ASCE)0733-9399(1998)124:8(892).

Leger, P. and Katsouli M. (1989), "Seismic stability of concrete gravity dams", *Earthq. Eng. Struct. D.*, **18**(6), 889-902. https://doi.org/10.1002/eqe.4290180611.

Lokke, A. and Chopra, A.K. (2018), "Direct finite element method for nonlinear earthquake analysis of 3-dimensional semi-unbounded dam-water-foundation rock systems", *Earthq. Eng. Struct. D.*, **47**(5), 1309-1328. https://doi.org/10.1002/eqe.3019.

Lotfi, V. (2004), "Direct frequency domain analysis of concrete arch dams based on FE-(FE-HE)-BE technique", *Comput. Concrete*, **1**(3), 285-302. https://doi.org/10.12989/cac.2004.1.3.285.

Lotfi, V (2009), "MAP-76: A program for analysis of concrete dams", Department of Civil & Environmental Engineering, Amirkabir University of Technology, Tehran, Iran.

Lotfi, V. and Abdorazaghi, H. (2024), "Dynamic analysis of Pine Flat dam–water–foundation rock system utilizing the H-W truncation boundary condition", *Eng. Comput.*, **41**(1), 131-154. https://doi.org/10.1108/EC-02-2023-0082.

Lotfi, V. and Espandar, R. (2002), "An investigation of joints behavior in seismic response of arch dams", *Electron. J. Struct. Eng.*, **1**(1), 17-31. https://doi.org/10.56748/ejse.222.

Lotfi, V. and Espandar, R. (2004), "Seismic analysis of concrete arch dams by combined discrete crack and non-orthogonal smeared crack technique", *Eng. Struct.*, **26**, 27-37, https://doi.org/10.1016/j.engstruct. 2003.08.007.

Lotfi, V. and Jahanitabar, A.A. (2024), "Application of single surface isotropic damage plasticity model in nonlinear dynamic analysis of the Koyna Dam", *Eng. Comput.*, **41**(6), 1602-1622. https://doi.org/10.1108/EC-02-2024-0108.

Lotfi, V. and Lotfi, A. (2021), "Application of Hagstrom-Warburton high-order truncation boundary condition on time harmonic analysis of concrete arch dam-reservoir systems", *Eng. Comput.*, **38**(7), 2996-3020, https://doi.org/10.1108/EC-08-2020-0441.

Lotfi, V. and Lotfi, A. (2022), "Time harmonic analysis of concrete arch dam-reservoir systems by utilizing GN high-order truncation condition", *Scientia Iranica*, **29**(6), 2825-2836. https://doi.org/10.24200/sci.2022.57180.5102.

Lotfi, V. and Omidi, O. (2012), "Dynamic analysis of the Koyna dam using three-dimensional plastic-damage modelling", *J. Dam Eng.*, **22**(3), 197-226.

Lotfi, V. and Samii, A. (2012), "Dynamic analysis of concrete gravity dam-reservoir systems by Wavenumber approach in the frequency domain", *Earthq. Struct.*, **3**(3-4), 533-548. https://doi.org/10.12989/eas.2012.3.3.533.

Lotfi, V. and Shiehnezhad, A. (2023), "Nonlinear dynamic analysis of concrete gravity dams by a simplified non-associated elasto-plastic joint model", *Submitted to the Journal of Scientia Iranica*.

Lotfi, V. and Zenz, G. (2018), "Application of Wavenumber-TD approach for time harmonic analysis of concrete arch dam-reservoir systems", *Coupled Syst. Mech.*, **7**(3), 353-371. https://doi.org/10.12989/csm.2018.7.3.353.

Lotfi, V. and Zenz, G. (2019), "Time harmonic analysis of concrete gravity dam-reservoir systems by Wavenumber-TD approach", *J. Dam Eng.*, **30**(2), 41-63.

Nasiri, F., Javdanian, H. and Heidari, A. (2020), "Seismic response analysis of embankment dams under decomposed earthquakes", *Geomech. Eng.*, **21**(1), 35-51. https://doi.org/10.12989/gae.2020. 21.1.035.

Omidi, O. and Lotfi, V. (2017), "Seismic plastic–damage analysis of mass concrete blocks in arch dams including contraction and peripheral joints", *Soil Dyn. Earthq. Eng.*, **95,** 118-137. https://doi.org/10.1016/j.soildyn.2017.01.026.

Samii, A. and Lotfi, V. (2012), "High-order adjustable boundary condition for absorbing evanescent modes of waveguides and its application in coupled fluid-structure analysis", *Wave Motion*, **49**(2), 238-257. https://doi.org/10.1016/j.wavemoti.2011.10.001.

Soysal, B.F., Binici, B. and Arici, Y. (2016), "Investigation of the relationship of seismic intensity measures and the accumulation of damage on concrete gravity dams using incremental dynamic analysis", *Earthq. Eng. Struct. D.*, **45**(5), 719-737. https://doi.org/10.1002/eqe.2681.

Soysal, B.F. and Arici, Y. (2024), "Crack width – seismic intensity relationships for concrete gravity dams", *J. Earthq. Eng.*, **28**(2), 565-581. https://doi.org/10.1080/13632469.2023.2220048.

Westergaard, H.M. (1933), "Water pressures on dam during earthquakes", *T. Am. Soc. Civil Engineers*, **98**(2), 418-433. https://doi.org/10.1061/TACEAT.0004496.

Wilson, E.L. (2002), "Three dimensional static and dynamic analysis of structures", *Computers and Structures*, Berkeley, California.

CC